Sustainable Engineering Novit
https://www.sciltp.com/journals/sen

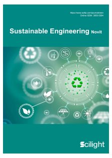

Review

Electrocatalytic Depolymerization of PET Plastic Fibers for Circular Textiles

Ruchuan Chen [1,†], Junfeng Li [1,†], Kean Zhu [1,†], Aoxiang Zhu [1], Weilin Xu [1], Hui Wang [2,*] and Jun Wan [1,*]

[1] State Key Laboratory of New Textile Materials and Advanced Processing, School of Chemistry and Chemical Engineering, Wuhan Textile University, Wuhan 430200, China
[2] School of Materials Science and Engineering, Nanyang Technological University, Singapore 639798, Singapore
* Correspondence: huiwang04@outlook.com (H.W.); wanj@wtu.edu.cn (J.W.)
† These authors contributed equally to this work.

How To Cite: Chen, R.; Li, J.; Zhu, K.; et al. Electrocatalytic Depolymerization of PET Plastic Fibers for Circular Textiles. *Sustainable Engineering Novit* **2026**, *2*(2), 6. https://doi.org/10.53941/sen.2026.100011

Received: 4 February 2026
Revised: 3 April 2026
Accepted: 14 May 2026
Published: 30 June 2026

Abstract: Poly (ethylene terephthalate) (PET) fibers constitute the largest share of global PET and are central to textiles and technical fabrics, yet high crystallinity, strong orientation, and complex finishing make them resistant to degradation and major sources of persistent microplastics. Conventional routes such as mechanical reprocessing, thermal depolymerization, hydrolysis, and alcoholysis were adapted from bulk PET but are inefficient for fibers due to limited accessibility, surface barriers, and poor selectivity toward high-purity monomers. This review adopts a fiber-centered perspective on electrocatalytic PET degradation that integrates structural, interfacial, and process considerations. It compares multiscale structural and chemical differences between fibers and bulk PET, and analyzes how pretreatments such as desizing, swelling, and surface activation condition fibers for electrochemical reactivity. It outlines fundamental principles of electrocatalytic depolymerization and classifies catalysts by structural descriptors including crystallinity, composition, and interfaces, supported by a consolidated dataset. Distinct from previous surveys, the review foregrounds fiber-specific interfaces and pretreatments and proposes a structure-centric framework for catalyst design. Highlights include transferable descriptors for cross-comparison and explicit coupling of pretreatment with catalyst selection. Looking ahead, priority is placed on scalable, continuous electrocatalytic platforms that link renewable electricity with circular textile recycling.

Keywords: PET; plastic fiber; electrocatalytic degradation; fiber pretreatment; plastic recycling

1. Introduction

Poly(ethylene terephthalate) (PET) fibers represent one of the most ubiquitous synthetic polymeric materials, underpinning large-scale applications in textiles, packaging, filtration, and functional composites. Their dominance arises from the combination of mechanical robustness, chemical resistance, low density, and processability into high-performance yarns and fabrics. However, the same features that make PET fibers indispensable in modern industries also render them highly persistent in natural and anthropogenic environments. The annual production of PET-based textiles has surpassed tens of millions of tons, and disposal after short usage cycles increasingly contributes to solid waste accumulation and microplastic release. Unlike amorphous or bulk PET used in bottles and films, fibrous PET exhibits hierarchical crystallinity, high orientation, and specific interfacial modifications which significantly complicate degradation pathways, reflecting the broader importance of structure–interface coupling in fiber-based functional materials introduced during spinning, drawing, and finishing, which significantly complicate degradation pathways [1]. Conventional disposal strategies, including mechanical recycling, thermal cracking, and chemical depolymerization, have demonstrated limited effectiveness when directly applied to fiber forms [2]. Mechanical recycling often leads to chain scission and inferior mechanical performance, while thermolysis requires high energy input and produces complex product mixtures. Hydrolysis and alcoholysis can, in principle, depolymerize PET into monomers, yet in practice the dense crystalline lamellae and additives in fibers hinder reagent penetration reduce conversion efficiency, a limitation commonly observed in highly ordered or functionally finished fiber systems [3] and reduce conversion efficiency [4]. As a result, an urgent need has emerged for more selective, energy-efficient, and fiber-compatible degradation strategies [5], fiber-compatible degradation strategies, which increasingly motivates structure- and process-engineered approaches rather than purely chemistry-driven routes [6,7]. This challenge has motivated a growing research effort aimed at identifying routes that not only achieve complete breakdown of PET fibers into high-purity monomers, but also address critical barriers such as crystallinity-driven resistance, interface-related mass transfer, and the presence of dyes and finishing agents [8].

Electrocatalysis offers a route to depolymerize PET fibers by converting electrical energy into a controllable chemical driving force at the fiber–electrolyte–electrode interface [9]. At this boundary, electron transfer and interfacial reactive species enable selective cleavage of ester linkages under relatively mild conditions, offering a promising avenue to construct energy-saving hybrid systems that replace conventional water oxidation for cost-effective hydrogen production [10]. In practice, mainstream schemes fall into a small set of tunable platforms, where advances in microwave-enabled synthesis and rapid structural engineering have provided versatile catalyst architectures [11,12]: anodic advanced oxidation generates surface-confined hydroxyl radicals and related oxidants on high-overpotential anodes; electro-Fenton cycles produce H_2O_2 and ·OH at cathodes while regenerating redox mediators; peroxymonosulfate or persulfate activation yields SO_4^{-}/·OH through either electrochemical reduction or catalytic pathways; cathodic routes supply adsorbed hydrogen and local alkalinity that accelerate alcoholysis or hydrolysis; photoelectrocatalytic hybrids expand interfacial charge separation and radical budgets; flow-through or three-dimensional electrodes increase accessible area and convective transport [13]. These platforms promise advantages that are particularly relevant to fibers: reactor-level control of driving force via potential or current density, aqueous processing with modest temperatures, compatibility with renewable electricity, and product streams that can be biased toward terephthalic acid (TPA), bis(2-hydroxyethyl) terephthalate (BHET), and ethylene glycol (EG) while tracking energy per treated mass $E_{sp} = (UIt)/m_{PET}$, Faradaic efficiency (FE), and selectivity S_i. Yet the literature remains fragmented in two critical respects that are specific to fiber geometries rather than films or flakes. First, the preconditioning of textiles has not been standardized. This includes desizing and de-finishing to remove dyes, TiO_2 matting agents, and metal residues. It also involves controlled swelling with EG, ionic liquids, or deep eutectic media, as well as treatments such as microfibrillation, plasma, ozone, UV activation, alkaline etching, or partial derivatization to increase amorphous accessibility. These steps determine effective surface area, wettability, local pH, and penetrant diffusion, which in turn govern the Damköhler number and ultimately define the attainable selectivity window for breaking ester bonds while preserving the aromatic ring. Second, catalyst development is still largely cataloged by material family rather than by transferable structural descriptors that should guide performance on fibers: band-edge and O-2p positions controlling oxidant generation, vacancy formation energies and lattice oxygen mobility dictating radical flux, Schottky or p–n junction barriers steering charge transfer, site density and pore connectivity setting interfacial kinetics versus transport, and Young–Dupré wetting work regulating three-phase line length on real yarn bundles. Without a fiber-aware pretreatment map and a structure-centric design grammar for electrocatalysts, comparisons across studies remain noncommensurate and scale-up to dyed, finished, and mixed-blend textiles is impeded despite promising bench-scale results.

This review aims to provide a comprehensive and fiber-oriented overview of electrocatalytic strategies for PET degradation that goes beyond conventional plastic-focused discussions [14]. Unlike previous reviews that primarily emphasize bulk PET or generalized electrocatalytic systems, this work highlights the structural, interfacial, and processing features that are intrinsic to fibers and critically influence degradation outcomes. The framework of this review is organized into four major components (Figure 1). The first part establishes the fundamental background by comparing the multiscale structural characteristics of PET fibers with bulk PET, outlining the interfacial complexity introduced during manufacturing and finishing, and evaluating the limitations of conventional recycling routes when applied to fibrous forms. The second part introduces the emerging field of electrocatalytic PET fiber degradation, focusing on definitions and scope, fiber pretreatment strategies that condition reactivity, reaction principles formulated through representative equations, and a structural classification of electrocatalysts based on crystallinity, composition, and interfaces, followed by a data-driven summary of reported systems. The third part examines case studies of catalyst families such as metals and alloys, oxides, hydroxides, sulfides, and phosphides, and also considers emerging materials including carbon-based frameworks, single-atom systems, and metal organic architectures, highlighting their performance, limitations, and relevance to fiber degradation. Finally, the review concludes with a synthesis of current progress, identification of key scientific and technological challenges, and forward-looking perspectives that emphasize fiber-compatible pretreatment, structure-guided catalyst design, and the integration of continuous and scalable electrochemical platforms. Through this structure-centered and fiber-specific lens, the review seeks to bridge existing gaps, distill generalizable insights, and provide a roadmap for advancing electrocatalytic PET fiber degradation toward practical and sustainable implementation. In summary, this review provides a fiber-centered perspective that synthesizes current advances in electrocatalytic PET degradation by integrating structural, interfacial, and processing considerations specific to fibrous systems. By organizing existing studies through unified descriptors and highlighting the coupling between pretreatment strategies and catalyst design, it aims to clarify structure–performance relationships and outline general principles to guide future research in fiber-specific recycling technologies.

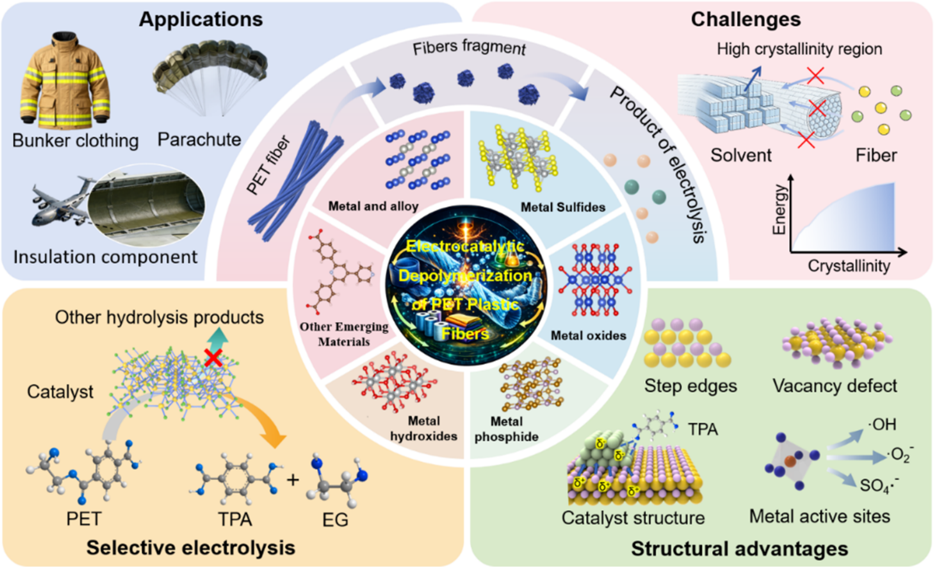

Figure 1. Schematic illustration of electrocatalytic depolymerization of PET fibers, highlighting application scenarios, reaction challenges, product pathways, and catalyst-related structural features.

2. Concepts and Conventional Strategies for PET Fiber Degradation

This section establishes the conceptual foundation and reviews conventional strategies for PET fiber degradation, providing the necessary background before addressing electrocatalytic approaches. It first examines the multiscale differences between PET fibers and bulk PET, emphasizing how crystallinity, molecular orientation, and hierarchical assembly into yarns and fabrics create unique structural and transport challenges. It then considers the interfacial complexity introduced during fiber manufacturing and finishing, where additives, dyes, and surface treatments modify accessibility and reactivity, thereby influencing degradation efficiency and selectivity. Finally, it surveys conventional chemical recycling routes, analyzing their mechanistic principles as well as their limitations when applied to fibrous architectures. Together, these discussions highlight why PET fibers cannot be treated simply as bulk PET, and why fiber-specific structural, interfacial, and process variables must be recognized as primary determinants of degradation outcomes.

2.1. Multiscale Differences between PET Fibers and Bulk PET

Poly(ethylene terephthalate) in its fibrous form occupies a critical position in contemporary materials use, distinct from the more widely recognized applications of PET in bottles, films, or packaging. Fibers account for more than half of global PET consumption, being the backbone of textiles for clothing, home furnishings, technical fabrics, industrial filters, geotextiles, and even biomedical scaffolds [15–17]. Their appeal derives from a unique combination of tensile strength, abrasion resistance, dyeability, and dimensional stability, which allows PET fibers to dominate both consumer and high-performance markets. In advanced contexts, they are integrated into protective garments, composite reinforcements, thermal insulation layers, and smart textiles with electronic or photonic functionalities [18,19]. The scale of this deployment makes PET fibers not only economically indispensable but also environmentally consequential: once incorporated into woven and nonwoven products, they enter waste streams after relatively short life cycles and become significant contributors to persistent microplastic release [20–22]. These fibers resist environmental degradation far more stubbornly than amorphous PET films because of their crystalline order and surface modifications, leading to accumulation in soil, water, and even atmospheric environments [23]. Consequently, developing efficient degradation and recycling pathways for PET fibers is not merely an extension of plastic management, but an urgent challenge with direct implications for resource recovery, pollution mitigation, and the sustainable circular economy of textile industries [24].

From a structural and processing standpoint, PET fibers differ fundamentally from bulk PET products such as bottles, sheets, or films, and these differences have profound implications for degradation behavior [25]. Bulk PET is typically produced with moderate crystallinity and relatively isotropic morphology, making depolymerization reactions more uniform and less hindered by anisotropic transport. In contrast, PET fibers undergo melt spinning, drawing, and heat setting, which generate a hierarchical architecture characterized by high degrees of molecular orientation, finely tuned crystalline–amorphous lamellae, and tightly packed fibrillar domains. This alignment enhances tensile strength and dimensional stability but also restricts reagent penetration and limits accessibility of ester linkages to hydrolytic or oxidative attack [26]. Moreover, the surface chemistry of fibers is frequently modified through finishing treatments, including dye uptake, incorporation of matting agents such as TiO_2, and application of coatings for flame retardancy, ultraviolet resistance, or hydrophobicity. These additional layers create interfacial barriers, introduce chemical heterogeneity, and can release inhibitory or interfering species during degradation. As a result, while bulk PET can often be processed through conventional hydrolysis, glycolysis, or thermolysis under relatively standardized conditions, fibrous PET resists these routes due to its multiscale ordering and interfacial complexity. Effective degradation strategies must therefore address both molecular-level crystallinity and macroscale fiber assemblies, making PET fibers not only more challenging but also more scientifically instructive as a testbed for advanced catalytic and electrochemical recycling approaches.

2.2. Interfacial Complexity from Manufacturing and Finishing of Fibers

During manufacturing, PET fibers acquire a complex interfacial architecture that fundamentally distinguishes them from bulk PET and directly influences their degradability [27]. The spinning and drawing processes induce high molecular orientation and crystallinity gradients from the fiber core to the surface, creating anisotropic domains that control accessibility to chemical or electrochemical agents. Rapid quenching during melt spinning often traps residual stresses and generates heterogeneous amorphous fractions, while subsequent drawing aligns chains into extended conformations that pack into lamellar crystallites [28,29]. Heat setting further stabilizes these arrangements, reducing segmental mobility at the interface [30]. In addition, industrial production often adds substances into the fiber matrix, including antimony catalysts, thermal stabilizers, and delustering agents, and these components can migrate to or accumulate on fiber surfaces. These inclusions alter surface polarity, electrostatic charge distribution, and defect density, thereby shaping how electrolytes, oxidants, and radicals interact during degradation. The result is a multilayered and nonuniform interfacial landscape where localized crystalline regions, additive-rich zones, and amorphous pockets coexist. Such heterogeneity complicates predictive modeling of degradation kinetics, because reaction initiation depends not only on bulk chemistry but also on micro- and nanoscale domains formed during manufacturing.

Finishing processes add yet another layer of interfacial complexity to PET fibers, as they involve deliberate surface modifications that tailor fiber performance but simultaneously create new barriers to degradation [31]. Dyeing treatments embed organic chromophores and auxiliaries into amorphous regions, introducing molecules with high aromatic stability and variable polarity that alter both adsorpted behavior and radical reactivity during chemical or electrochemical attack. The incorporation of inorganic matting agents such as TiO_2 particles modifies light scattering and surface energy but also generates heterogeneous nucleation sites and micropores that complicate reagent penetration. Functional finishing agents, including flame retardants, ultraviolet absorbers, antimicrobial coatings, water- and oil-repellent layers, and antistatic treatments, form thin interfacial films or chemically bonded layers that shield underlying ester groups from reactive species. In many cases, these finishes also introduce elements such as halogens, phosphorus, or heavy metals, which can either quench reactive intermediates or catalyze side reactions, thereby reducing selectivity and energy efficiency in degradation pathways. Moreover, finishing is rarely uniform across a textile assembly: differences between filament surfaces, yarn junctions, and fabric interstices create gradients in wettability, porosity, and chemical composition. This spatial heterogeneity magnifies the challenge of designing effective degradation processes, as catalytic or oxidative systems must not only target ester bonds in the PET backbone but also overcome or even exploit diverse surface chemistries that are integral to the fiber's end-use performance.

2.3. Conventional Chemical Recycling Pathways

Conventional chemical recycling of PET fibers relies primarily on depolymerization pathways such as hydrolysis, alcoholysis, glycolysis, methanolysis, and, more recently, enzymatic degradation, yet each of these routes exhibits distinctive advantages and persistent shortcomings when applied to fibrous architectures. Hydrolysis, carried out under acidic, alkaline, or neutral conditions, can theoretically yield TPA and EG with high purity, but the dense crystalline lamellae and molecular orientation of fibers significantly limit reagent penetration, resulting in incomplete depolymerization and long reaction times (Figure 2). Alcoholysis, including glycolysis and methanolysis, introduces alcohols such as EG or methanol to generate BHET or dimethyl terephthalate (DMT), which are useful monomers for repolymerization; however, the effectiveness of these processes is reduced in fibers because additives, dyes, and finishes alter local polarity and act as side reaction sites [32–34]. Thermal depolymerization through pyrolysis or gasification avoids solvent use but requires elevated temperatures that accelerate secondary reactions, producing complex product mixtures, tars, and gaseous by-products, which complicate downstream purification [35,36]. Enzymatic degradation, exemplified by cutinase- and PETase-based systems, has attracted attention for its mild operating conditions and potential selectivity, yet its efficiency remains strongly inhibited by high crystallinity and the compact morphology of fibers, where enzymes cannot easily access buried ester linkages. In all these approaches, additional complications arise from the heterogeneous composition of real textile waste, including blended fabrics, residual metals from catalysts, and surface coatings that block reactive sites or release inhibitors [37]. As a result, although conventional chemical pathways provide a theoretical basis for closing the PET cycle, their direct translation to fibrous substrates remains inefficient and energy-intensive, highlighting the necessity of developing new strategies that integrate fiber-specific pretreatment, improved catalyst design, and selective reaction environments [38,39].

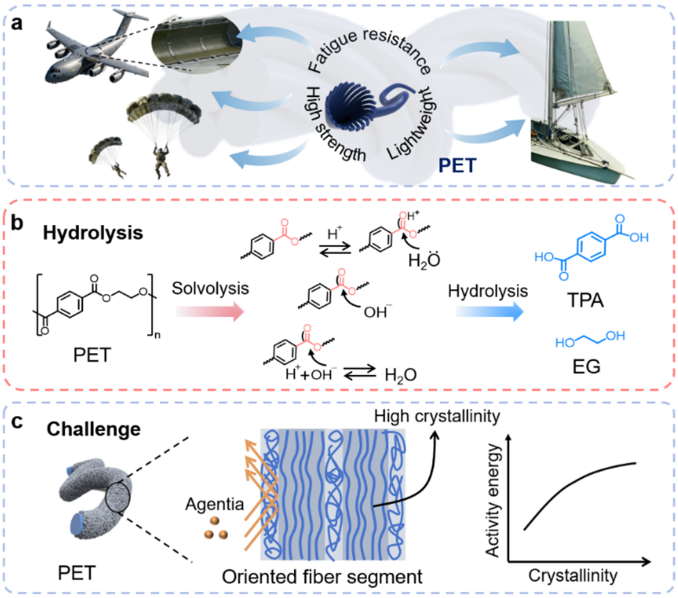

Figure 2. Schematic overview of conventional PET recycling routes and fiber-architecture-related limitations: (**a**) applications of PET fibers; (**b**) hydrolysis-based depolymerization pathways, and (**c**) crystallinity-induced accessibility constraints.

3. Electrocatalytic Degradation of PET Fibers

Electrocatalytic degradation has recently emerged as a fiber-specific strategy for PET recycling, and the discussion is organized around several interrelated dimensions. It first clarifies the definitions and scope of electrocatalysis in this context, distinguishing it from conventional electrochemical processes and highlighting the potential advantages of using applied potentials and catalyst interfaces to drive selective ester bond cleavage under mild conditions. It then examines fiber pretreatment strategies, emphasizing how desizing, de-finishing, swelling, and surface activation can fundamentally reshape accessibility, wettability, and crystallinity, thereby determining the efficiency of subsequent electrochemical reactions [40]. Building on this foundation, the section presents a macroscopic account of the underlying reaction mechanisms and principles, framed through representative equations and kinetic considerations rather than subdivided mechanistic categories, in order to capture the general features of radical generation, interfacial charge transfer, and mass transport in fibrous assemblies. The discussion then turns to structural features of electrocatalysts, categorized not by material families but by crystallinity, composition, and interface characteristics, with the goal of identifying descriptors that can rationally guide catalyst design for fiber degradation. Finally, the section consolidates reported studies into a standardized summary of catalyst types, electrolytes, operating conditions, and performance metrics, allowing cross-comparison and enabling the identification of emerging structure–performance relationships that can inform future research.

3.1. Definitions and Scope of Electrocatalytic PET Fiber Degradation

Electrocatalytic degradation of PET fibers can be broadly defined as the process in which applied electrical energy, mediated through catalyst–electrolyte–fiber interfaces, drives selective cleavage of ester linkages in the polymer backbone under aqueous or mixed solvent conditions. Unlike conventional electrolysis, where electrodes may simply generate reactive intermediates in bulk solution, electrocatalysis relies on tailored catalytic surfaces that regulate electron transfer, adsorb polymer fragments, and control the generation of oxidizing or reducing species to enhance efficiency and selectivity [41] (Figure 3a). To avoid conceptual confusion, it is essential to distinguish between electrocatalysis and electrochemical oxidation in the context of PET degradation. Traditional electrochemical oxidation typically relies on the non-selective attack of electro-generated radicals or direct electron transfer at high-overpotential anodes, aiming for the aggressive breakdown and often mineralization of polymers. Its application scope is generally focused on the remediation of microplastics or deep degradation of recalcitrant fragments. Conversely, electrocatalysis involves the specific adsorption of the PET backbone or its soluble intermediates onto the catalyst's active sites, which modulate the reaction coordinate to enable selective ester bond cleavage or the valorization of depolymerization products. By establishing this distinction, the specific role of tailored catalyst surfaces in steering selectivity can be better isolated from non-selective oxidative processes. The scope of this approach encompasses several unique advantages that are particularly relevant to fibers. First, the external potential provides a tunable driving force that enables reaction pathways to be modulated without the need for excessive thermal or chemical inputs, reducing both energy demand and solvent burden. Second, the electrocatalytic interface creates localized microenvironments where hydroxyl radicals, sulfate radicals, or adsorbed hydrogen species are produced in situ, allowing ester scission to occur directly at the fiber–electrolyte boundary rather than through non-selective bulk reactions [42–44]. Third, the method is inherently compatible with renewable electricity, offering a sustainable route for polymer valorization that aligns with circular economy objectives [45,46]. Importantly, when applied to PET fibers, electrocatalysis addresses challenges that cannot be resolved by traditional recycling routes: crystalline lamellae, oriented fibrils, and surface finishes can all hinder conventional depolymerization but can be overcome by combining fiber pretreatment with catalytic control at the electrode. Thus, the definition of electrocatalytic PET fiber degradation extends beyond simple monomer recovery; it frames a platform where catalyst design, interface engineering, and process scalability converge to transform resistant fibrous waste into valuable chemical feedstocks in an energy-efficient and environmentally responsible manner.

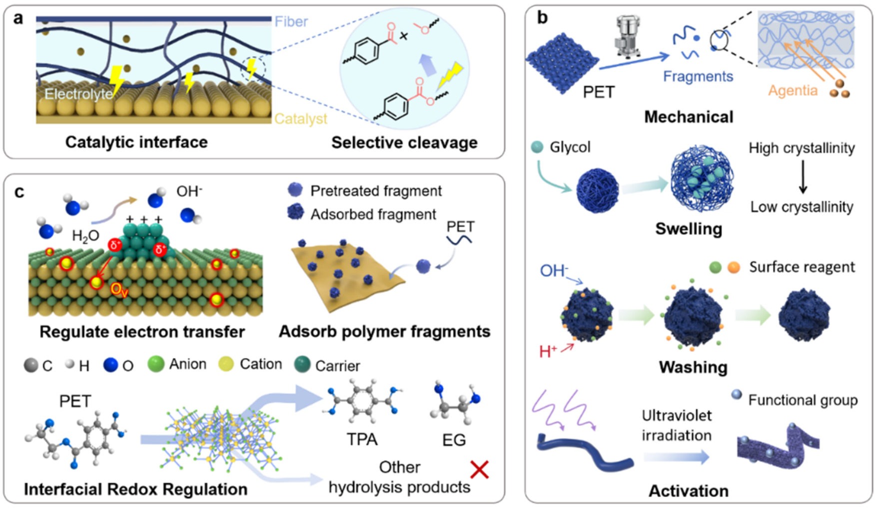

Figure 3. Schematic overview of electrocatalytic PET fiber depolymerization: (**a**) catalyst–electrolyte–fiber interfacial microenvironment; (**b**) pretreatment strategies; and (**c**) interfacial redox regulation.

3.2. Pretreatment Strategies of PET Fibers for Enhanced Electrocatalytic Degradation

Pretreatment of PET fibers is a decisive step for effective electrocatalytic degradation because it directly determines the accessibility of ester bonds. Additionally, pretreatment enhances the quality of the fiber–electrolyte–

catalyst interface, which ultimately governs the kinetics of subsequent electrochemical reactions [47,48]. Unlike bulk PET films or flakes, fibers exhibit high crystallinity, strong molecular orientation, and complex finishing layers, all of which severely restrict reagent diffusion and radical penetration. Pretreatment strategies therefore aim to disrupt these barriers, increase the fraction of amorphous domains, and expose reactive groups without excessively compromising fiber integrity (Figure 3b). Mechanical routes such as fibrillation, shredding, or cryogenic milling reduce fiber diameter and increase surface area, while simultaneously enhancing the diffusion of electrolyte into inner domains, highlighting how manufacturing-enabled structural control can be leveraged to tune functional accessibility [49,50]. Chemical swelling treatments using EG, ionic liquids, or deep eutectic solvents can loosen intermolecular packing and decrease crystallinity, thereby lowering the activation barrier for ester scission, analogous to how rapid synthesis of porous architectures enhances mass transport and active-site exposure in functional oxides [51]. Alkaline or acidic washing, combined with desizing and de-finishing, removes dyes, catalysts, and hydrophobic coatings that otherwise block electron transfer and quench reactive intermediates. Surface activation techniques, including plasma, ozone, and UV irradiation, introduce polar functional groups and surface roughness that improve wettability and promote electrochemical contact. More advanced approaches involve partial derivatization of ester groups to generate more labile intermediates, or incorporation of redox-active additives that enhance interfacial charge transfer during electrocatalysis. Each pretreatment pathway alters key structural descriptors such as crystallinity, contact angle, accessible surface area, and interfacial chemical composition [52]. As a result, these changes directly affect degradation selectivity and energy efficiency.

To illustrate this effect with quantitative evidence, recent literature shows that removing organic spin finishes from PET fibers through solvent extraction can lower charge transfer resistance and increase the Faradaic Efficiency for ethylene glycol electro-oxidation to formate by 15%, reaching over 90%. Similarly, the decolorization of dyed textiles through reductive clearing has been reported to eliminate competitive adsorption on active sites, resulting in a specific reduction in overpotential of approximately 45 millivolts at a current density of 10 milliamperes per square centimeter during degradation [53,54].

Consequently, pretreatment should not be considered as an auxiliary operation but rather as an integral design parameter for electrocatalytic PET fiber recycling, with the potential to transform otherwise intractable fibrous waste into substrates that respond predictably to catalytic control.

3.3. Reaction Mechanisms and Fundamental Principles of Electrocatalytic Degradation

The reaction mechanisms underlying electrocatalytic degradation of PET fibers can be understood as the interplay between interfacial electron transfer, generation of reactive species, and mass transport within the hierarchical fiber structure (Figure 3c) [55]. From a mechanistic perspective, these processes can be broadly categorized into two distinct pathways depending on whether polymer chain scission occurs directly on the solid substrate or proceeds through soluble intermediates. The first pathway involves direct electrocatalytic depolymerization of PET fibers, in which reactive species generated at the electrode interface attack ester bonds within the polymer matrix, leading to the formation of products such as terephthalic acid and ethylene glycol. This route is strongly influenced by interfacial accessibility, crystallinity, and mass transport limitations within the fibrous structure. The second pathway, which accounts for a large proportion of highly efficient conversions reported in the current literature, follows a sequential process consisting of an initial alkaline hydrolysis step to generate ethylene glycol, followed by electrocatalytic oxidation of ethylene glycol into value-added products such as formic acid or glycolic acid using specific catalysts, including Pd-based and Ni-based systems [56]. In this case, the overall efficiency is largely governed by the kinetics of small-molecule electrooxidation rather than direct polymer depolymerization. This pathway also provides a natural basis for paired electrolysis, where the anodic oxidation of PET-derived intermediates can be coupled with a complementary cathodic reaction, thereby improving overall energy efficiency and reducing energy consumption [57].

Within these two pathways, at the electrode surface, applied potentials initiate redox reactions that yield oxidizing and reducing intermediates, including hydroxyl radicals ($\cdot OH$), sulfate radicals (SO_4^-), hydrogen peroxide, and adsorbed hydrogen species, which play a central role in the oxidative degradation of organic substrates through interfacial electron transfer processes [58]. These species attack the carbonyl groups of PET, promoting hydrolytic or oxidative scission of the ester linkage, with TPA, BHET, and EG as the main products. The reaction can be summarized in simplified form as $[-O-CH_2-CH_2-O-CO-Ph-CO-]_n + nH_2O + ne^- \rightarrow nTPA + nEG$, although in practice the process proceeds through multiple intermediates, including mono-hydroxyethyl terephthalate (MHET) and oligomeric fragments [59–61]. Importantly, the kinetics of these transformations are governed not only by intrinsic electron-transfer rates but also by diffusion limitations associated with crystalline lamellae and surface finishes, which restrict penetration of reactive species into the fiber interior [62–64]. Consequently, the Damköhler number and Thiele modulus provide useful descriptors for distinguishing between surface-reaction-limited and transport-limited regimes in fiber assemblies [65,66]. Selectivity is another critical principle: mild oxidative potentials can preferentially cleave ester bonds while preserving aromatic rings, whereas uncontrolled radical flux may over-oxidize to CO_2 or generate colored by-products that complicate monomer recovery [67]. Energy efficiency, typically quantified as specific energy consumption per unit mass treated, is also strongly linked to electrode potential, catalyst structure, and electrolyte composition, underscoring the need for finely tuned operating windows [68–70]. Overall, the fundamental principles of electrocatalytic PET fiber degradation integrate interfacial electrochemistry with polymer science, demonstrating that effective recycling requires simultaneous optimization of electron-transfer pathways, radical generation, and transport through the multiscale architecture of fibers [71].

3.4. Structural Features of Electrocatalysts including Crystallinity, Composition, and Interfaces

Crystallinity serves as a pivotal structural determinant in the electrocatalytic degradation of PET fibers. It primarily governs the density, accessibility, and electronic properties of active sites on the electrode surface. Recent investigations emphasize that meticulous engineering of the material’s phase and crystallinity can fundamentally reconfigure its surface redox kinetics (Figure 4) [72]. Highly crystalline catalysts, such as ordered metal oxides and spinel structures, typically offer well-defined lattice arrangements that stabilize high-valence states and facilitate the generation of reactive oxygen species under anodic polarization [73–75]. The inherent periodicity and long-range structural order of these catalysts effectively reduce the energy barrier for continuous redox cycling. Consequently, this structural stability facilitates the accelerated generation of reactive oxygen species, such as hydroxyl and sulfate radicals, which are essential for cleaving the ester linkages in PET fibers. However, excessive crystallinity may also reduce the density of surface defects, oxygen vacancies, or undercoordinated metal centers that are often crucial for enhancing catalytic activity and selectivity complex reaction environments [76–78]. In contrast, catalysts with lower crystallinity or partially amorphous domains exhibit higher defect concentrations and larger accessible surface areas, which can improve adsorption of polymer fragments and accelerate electron transfer [79]. Yet such disorder may compromise structural stability and durability under repeated cycling. Therefore, an optimal balance between crystalline order and defect-mediated reactivity is essential, where the catalyst maintains sufficient structural integrity to resist dissolution or deactivation while offering the lattice flexibility and surface heterogeneity needed to accommodate diverse reaction intermediates generated during PET fiber depolymerization.

Composition represents another central determinant of electrocatalyst performance in PET fiber degradation, as the elemental identity, stoichiometry, and heteroatom incorporation collectively regulate both electronic structure and surface chemistry [80,81], as exemplified by solid-solution strategies that enable continuous tuning of electronic and defect states [82]. Transition metals such as cobalt, nickel, manganese, and iron are widely employed because their variable oxidation states and d-orbital configurations enable efficient redox cycling and radical generation. Binary or multicomponent systems, including perovskites, spinels, and layered double hydroxides, introduce synergistic effects where one component stabilizes high-valence centers while another enhances conductivity or oxygen vacancy formation, thereby improving both activity and stability. Incorporation of nonmetals such as nitrogen, sulfur, or phosphorus can further tailor the local coordination environment, shifting band positions and modulating charge density at active sites to favor selective ester bond cleavage over non-productive oxidation [83–85]. Single-atom catalysts exemplify the extreme end of compositional precision, where isolated metal centers coordinated by nitrogen or oxygen atoms provide uniform, high-turnover sites with well-defined adsorption geometries for PET-derived intermediates [86,87]. In addition, compositional tuning affects tolerance toward dyes, finishing agents, and metal impurities commonly present in textile waste: for example, catalysts with strong metal–support interactions or heteroatom anchoring can mitigate deactivation caused by contaminant adsorption. Thus, rational control of composition not only dictates intrinsic electrocatalytic properties but also determines the resilience of the system in real-world fiber degradation scenarios.

Interfaces form the critical junction where electrocatalysts, electrolytes, and PET fibers interact, and their structural characteristics often dictate the overall efficiency and selectivity of degradation [88,89], reflecting the broader role of interfacial synergy and electronic coupling in stabilizing active configurations [90,91]. Unlike bulk properties, interfacial features determine how electrons, ions, and reactive intermediates are transferred and confined within the local reaction environment [92]. Heterojunctions between semiconducting oxides, metals, or carbonaceous phases can establish built-in electric fields that promote charge separation, suppress recombination, and enhance radical flux at controlled sites, directly influencing ester bond cleavage. Similarly, strong metal–support interactions stabilize active centers against leaching while tuning adsorption strength of intermediates such as BHET or TPA precursors, thereby guiding reaction pathways toward desired products [93]. Surface wettability and texturing add another layer of interfacial complexity: hydrophilic domains improve electrolyte penetration and contact with fiber bundles, whereas amphiphilic or patterned surfaces extend three-phase boundaries that enable simultaneous access to electrons, reagents, and polymer chains. At the same time, defects, step edges, and oxygen vacancies located at interfaces serve as preferential sites for radical generation, but if poorly controlled, they may catalyze nonselective oxidation and accelerate catalyst degradation. Therefore, the design of electrocatalysts for PET fiber degradation requires careful engineering of interfacial architectures. This includes atomic-scale coordination environments and mesoscale porous frameworks that together optimize charge transfer, mass transport, and selective adsorption while ensuring long-term structural stability in complex textile waste matrices [94,95].

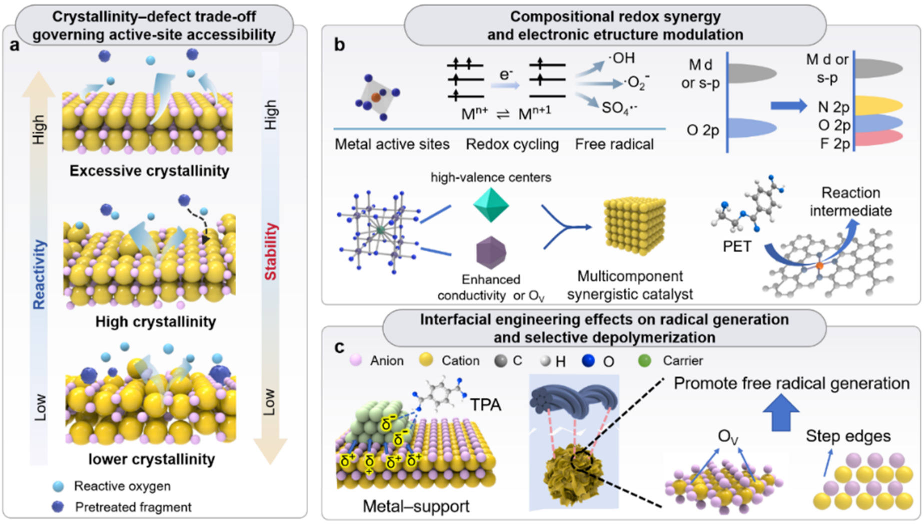

Figure 4. Schematic overview of key structural features governing electrocatalytic PET depolymerization. (**a**) Structural order and defect-mediated reactivity; (**b**) Compositional redox synergy and electronic etructure modulation; (**c**) Interfacial engineering effects on radical generation and selective depolymerization.

3.5. Summary and Analysis of Existing Electrocatalysts for PET Degradation

To enable a quantitative and mechanism-informed comparison across disparate electrocatalytic systems, Table 1 compiles reported catalysts, substrates, electrolytes, kinetic metrics, selectivity, and stability for PET or PET-derived electrochemical degradation, thereby revealing performance trends that are otherwise obscured by differing test conditions. From these data, metallic catalysts and alloys typically exhibit low to moderate overpotentials in alkaline electrolytes (often ~250–400 mV at 10–100 mA cm^{-2}) and high intrinsic activity, yet their Faradaic efficiencies span a broad range from ~70% to >95% and stability is frequently limited to tens of hours, consistent with surface oxidation and leaching under anodic bias. Metal oxides, including spinels and perovskites, generally require slightly higher overpotentials (commonly 300–500 mV at comparable current densities) but deliver more consistent selectivity, with formate or glycolate Faradaic efficiencies often exceeding 90% and operational stability extending beyond 30–50 h, reflecting the stabilizing role of lattice oxygen redox and mixed-valence cations. Metal hydroxides and layered double hydroxides occupy an intermediate regime, achieving current densities of 50–200 mA cm^{-2} at overpotentials as low as ~170–350 mV while maintaining Faradaic efficiencies around 85–95%, a behavior attributable to their abundant surface hydroxyls, alkaline interfacial microenvironments, and flexible cation substitution that lowers kinetic barriers for ester bond scission. Sulfides and phosphides frequently reach higher current densities, in some cases approaching or exceeding 300–500 mA cm^{-2}, but often at the expense of increased overpotential and variable stability, highlighting the trade-off between enhanced conductivity and susceptibility to surface reconstruction. Emerging materials define distinct performance windows: MOF-based catalysts and single-atom systems achieve markedly reduced onset potentials and high selectivity, with Faradaic efficiencies up to ~95–96% and improved Tafel slopes indicative of accelerated charge transfer, whereas boron-doped diamond electrodes operate at high overpotentials (>650 mV) yet drive near-complete mineralization, emphasizing efficiency–selectivity trade-offs. Electro-organocatalytic systems stand out by enabling PET depolymerization at very low effective overpotentials through single-electron transfer, albeit currently at lower current densities. Overall, the compiled data indicate that optimal electrocatalytic PET degradation does not correlate with catalyst class alone, but rather with how crystallinity, electronic structure, and interfacial chemistry jointly regulate achievable current density, selectivity, and durability, reinforcing the importance of structure-guided catalyst design tailored to specific degradation objectives.

Table 1. Comprehensive summary of structure-dependent electrocatalytic performance for PET degradation.

Material Classification	Catalyst	Degradation Substrate	Electrolyte	Overpotential @Current Density	FE [%]	Tafel Slope (mV dec^{-1})	Stability @Current Density	Substrate Source	Refs.
Metal oxide	$NiCo_2O_4$	EG	1.0 M KOH + 0.3 M EG	420 mV @100 mA cm^{-2}	98.9 (formate)	31.5	50 h @100 mA cm^{-2} (CP)	Polyester waste	[96]
	Pd/Fe–Nb_2O_5	EG	0.5 M KOH + 1.0 M EG	320 mV @10 mA cm^{-2}	100 (liquid products)	120	25 h @10 mA cm^{-2}	Commercial reagent	[97]
	$Ni_{0.5}Ce_{0.5}Co_2O_4$	EG	1.0 M KOH + PET hydrolysate	200 mV @ 100 mA cm^{-2}	95 (formate)	118	6 cycles @1.55 V vs RHE (CA)	Commercial PET Powder	[98]
	g-C_3N_4/Fe_2O_3/PdNPs	EG	0.5 M KOH + 0.5 M EG	220 mV @100 mA cm^{-2}	100 (liquid products)	120	100 cycles @50 mV s^{-1} (CV)	Commercial reagent EG	[99]
	CuO NWs-200 °C	EG	1.0 M KOH + PET hydrolysate	260 mV @10 mA cm^{-2}	88 (formate)	96	40 h @1.45 V vs RHE (CA)	Waste PET plastic	[100]
	Porous NiO/Ni-12@NF	EG	1.0 M KOH + 0.03 M EG	247 mV @100 mA cm^{-2}	45.5 (H_2)	120	1 h @1.51 V vs RHE (CA)	Commercial reagent EG	[101]
	Pd/Mn_3O_4/C	EG	2.0 M KOH + 2.0 M EG	580 mV @100 mA cm^{-2}	-	-	1 h @10 mA cm^{-2}	Commercial reagent EG	[102]
	Ni–PbO_2–GN/GC	EG	1.0 M NaOH + 1.0 M EG	380 mV @172 mA cm^{-2}	98	-	600 s @10 mA cm^{-2}	Commercial reagent EG	[103]
	Mesoporous Co_3O_4	EG	1.0 M KOH + 1.0 M EG	1.63 V @70 mA cm^{-2}	65 (glycolate + formate)	110	15 h @10 mA cm^{-2}	Commercial reagent EG	[104]
	R-Ni_3Co_1/NF	EG	1.0 M KOH + 0.1 M EG	264 mV @50 mA cm^{-2}	98.2 (FA)	54	24 h @10 mA cm^{-2}	Post-consumer PET	[105]
	Ti/Ru–Ir mixed metal oxide (MMO) anode	PET microplastics (also PE MPs)	0.1 M $NaClO_4$ + 1000 mg dm^{-3} Cl^-	650 mV @100 mA cm^{-2}	-	-	800 h @20 mA cm^{-2} (CP)	Commercial PET Powde	[106]
Metal and alloy	PdCu MCs	EG	1.0 M KOH + PET hydrolysate	830 mV @100 mA cm^{-2}	93.6 (GA)	110	10 cycles @0.83 V vs RHE (CA)	Commercial reagent EG	[107]
	Pt/C	EG	1.0 M KOH + 0.5 M EG	400 mV @38 mA cm^{-2}	95.0 (glycolic acid, AEM-DEGFC)	120	2 h @177 mA cm^{-2} (CA, AEM-DEGFC)	Commercial reagent EG	[108]
	PdCu/NF	EG	1.0 M KOH + 0.5 M EG	830 mV @740 mA cm^{-2}	99 (GA)	73	60 h @100 mA cm^{-2} (CP)	Polyester waste	[109]
	PdBi/NF	EG	1.0 M KOH + 0.5 M EG	0.90 V @150 mA cm^{-2}	99 (GA)	119.4	100 h @150 mA cm^{-2}(CP)	Reagent-grade EG	[110]
	LM-PdCu	EG	1.0 M KOH + 0.10 M EG	0.76 V @10 mA cm^{-2}	96.8 (GA)	58.4	9 h @10 mA cm^{-2}	Bottle PET	[111]
	$NiMoCo_{0.3}$ nanowire arrays @ NF	EG	1.0 M KOH + 0.10 M PET hydrolysate	1.40 V @200 mA cm^{-2}	93.5 (formate)	46.9	45 h @1.40 V vs RHE (CA)	Commercial PET Powde	[112]
	PdAg/NF	EG	0.5 M KOH + 1.0 M EG	570 mV @10 mA cm^{-2}	92 (GA)	252	2 h @0.91 V vs RHE (CA)	Commercial reagent EG	[113]
	$Pd_{67}Ag_{33}$ alloy aerogel	EG	1.0 M KOH + 1.0 M EG	530 mV @10 mA cm^{-2}	92.7 (GA)	157.1	80 h @1.0 V vs RHE (CA)	Commercial reagent EG	[114]
	PtRu/CNT	EG	0.5 M H_2SO_4+ 0.5 M EG	500 mV @100 mA cm^{-2}	92 (GA)	120	500 cycles @50 mV s^{-1} (CV)	Commercial reagent EG	[115]

Table 1. *Cont.*

Material Classification	Catalyst	Degradation Substrate	Electrolyte	Overpotential @Current Density	FE [%]	Tafel Slope ($mV\ dec^{-1}$)	Stability @Current Density	Substrate Source	Refs.
Metal and alloy	PdNiMo/C	EG	1.0 M KOH + 1.0 M EG	360 mV @100 mA cm^{-2}	87.7 (GA)	82	6 h @0.83 V vs RHE (CA)	Commercial reagent EG	[116]
	Au(polycrystalline disk)	EG	1.0 M NaOH + 1.0 M EG	100 mV @41.2 mA cm^{-2}	≈95 (GA)	118	2 h @1.00 V vs RHE (CA)	Commercial reagent EG	[117]
	N–PdRh@$Ni(OH)_2$/NF	EG	1.0 M KOH + 1.0 M EG	900 mV @1093 mA cm^{-2}	95.14 (GA)	179.12	12 h @60 mA cm^{-2}	Commercial reagent EG	[118]
Metal hydroxide	Pd@$Ni(OH)_2$–NiO/NF	EG	2.0 M KOH + 0.2 M EG	608 mV @300 mA cm^{-2}	91.7 (GA)	232.4	250 h @300 mA cm^{-2}	Commercial reagent EG	[119]
	$Ni_{0.9}Mn_{0.1}$LDH	EG	1.0 M KOH + 1.0 M EG	437 mV @10 mA cm^{-2}	85.8 (FA)	207	12 h @20 mA cm^{-2}	Commercial reagent EG	[120]
	CoV-LDH/NF	EG	1.0 M KOH + 0.15 M EG	1470 mV @350 mA cm^{-2}	86.61 (FA)	80.12	36 h @13 mA cm^{-2}	Commercial reagent EG	[121]
	$Ni(OH)_2$/MnO@Ni aerogel (NiMn AG)	EG	1.0 M KOH + 0.5 M EG	120 mV @10 mA cm^{-2}	96 (formate)	21.9	36 h @1.52 V vs RHE (CA)	Commercial reagent EG	[122]
	$Ni(OH)_2$ hollow nanospheres	EG	1.0 M KOH + 0.5 M EG	180 mV @10 mA cm^{-2}	92 (FA)	120	10 h @10 mA cm^{-2}	Commercial reagent EG	[123]
	Ru,S–$Ni(OH)_2$–OV	EG	1.0 M KOH + 0.5 M EG	210 mV @500 mA cm^{-2}	91.2 (FA)	99	75 h @100 mA cm^{-2}	Commercial reagent EG	[124]
	Pt–$Ni(OH)_2$/NF	EG	1.0 M KOH + 1.0 M EG	880 mV @250 mA cm^{-2}	90.1 (GA)	41.7	500 cycles (CV)	Commercial reagent EG	[53]
Metal phosphide	Pd–CoNiP@NF	EG	1.0 M KOH + 0.12 M EG	1310 mV @500 mA cm^{-2}	94.5 (FA)	56.5	5856 h @500 mA cm^{-2}	Commercial reagent EG	[125]
	OMS-Ni_1-CoP	EG	1.0 M KOH + 0.5 M EG	430 mV @10 mA cm^{-2}	96 (FA)	108.2	10 h @10 mA cm^{-2}	Commercial reagent EG	[126]
	Fe_2P–Co_2P@Cmp	EG	1.0 M KOH + 0.5 M EG	1.42 V @100 mA cm^{-2}	99.1 (FA)	87	16 h @500 mA cm^{-2}	Commercial reagent EG	[127]
	$CoNi_{0.25}P$/NF	EG	1.0 M KOH + 0.3 M EG	1.70 V @350 mA cm^{-2}	91.3 (FA)	58.1	39 h @10 mA cm^{-2}	Bottle PET	[128]
	PdNiP/C	EG	1.0 M KOH + 0.5 M EG	250 mV @10 mA cm^{-2}	95 (GA)	120	1000 s @10 mA cm^{-2}	Commercial reagent EG	[129]
	Co_2P–Ni_2P/CC	EG	1.0 M KOH + 0.5 M EG	1.30 V @100 mA cm^{-2}	90.6 (FA)	126.6	70 h @100 mA cm^{-2} (CP)	Commercial reagent EG	[130]
	CoFe-P/NF	EG	1.0 M KOH + PET hydrolysate	93 mV @10 mA cm^{-2}	90 (FA)	135	5 cycles @1.50 V vs RHE (CA)	Commercial reagent PET	[131]
	$Ni_{12}P_5$ nanoparticles	EG	1.0 M NaOH + 1.0 M EG	204 mV @20 mA cm^{-2}	98 (FA)	193	50 cycles (CV)	Commercial reagent EG	[132]
	Ru/Ni_2P/NF	EG	1.0 M KOH + 0.5 M EG	1.37 V @100 mA cm^{-2}	100 (CO_2)	120	30 h @10 mA cm^{-2}	Commercial reagent EG	[133]
	CoFe-P	EG	1.0 M KOH	200 mV @10 mA cm^{-2}	90 (FA)	35.2	2 h @10 mA cm^{-2}	Commercial reagent EG	[134]

Table 1. *Cont.*

Material Classification	Catalyst	Degradation Substrate	Electrolyte	Overpotential @Current Density	FE [%]	Tafel Slope (mV dec^{-1})	Stability @Current Density	Substrate Source	Refs.
Metal sulfide	Ni_3S_2@NiFeMn-LDH/NF	EG	1.0 M KOH + 1.0 M EG	60 mV @10 mA cm^{-2}	90 (FA)	113.7	8 h @10 mA cm^{-2}	Commercial reagent EG	[123]
	Ni–Co_9S_8 NSAs/NF	EG	1.0 M KOH + 1.0 M EG	50 mV @100 mA cm^{-2}	92 (FA)	120	24 h @10 mA cm^{-2}	Commercial reagent EG	[135]
Metal selenide	Branched $NiSe_2$ nanoparticles	EG	1.0 M KOH + 1.0 M EG	1.395 V @50 mA cm^{-2}	80 (formate)	125	10 h @10 mA cm^{-2}	Commercial reagent EG	[136]
Other emerging materials	Cobalt-based 1D coordination polymer (open metal sites)	EG	1.0 M KOH + PET hydrolysate	1.42 V @10 mA cm^{-2}	77 (FA/KDF)	117	6 h @10 mA cm^{-2}	Commercial reagent EG	[137]
	FeCo(MOF)@C	EG	1.0 M KOH + 0.5 M EG	1.42 V @100 mA cm^{-2}	90 (FA)	95	160 h @500 mA cm^{-2}	Commercial reagent PET	[138]
	Ni-based metal-organic frameworks (MOF)	EG	1.0 M KOH + 0.5 M EG	1.37 V @10 mA cm^{-2}	94 (formate)	35.1	20 h @10 mA cm^{-2}	Commercial reagent EG	[139]
	Tb-doped Co-MOF/NF	EG	1.0 M KOH + 0.5 M EG	200 mV @10 mA cm^{-2}	85 (FA)	31.5	2 h @10 mA cm^{-2}	Commercial reagent EG	[140]
	BDD (Boron-Doped Diamond)	PET	0.03 M Na_2SO_4	140 mV @10 mA cm^{-2}	81 ± 3	360	12 h @10 mA cm^{-2}	Commercial reagent PET	[141]
	$[N\text{-}DMBI]_2$ (Benzimidazolium)	PET	Acetonitrile (MeCN)	2.25 V @10 mA cm^{-2}	90	-----	Varies, stable with mediator up to 90% yield	Commercial reagent PET	[142]
	Electro-generated •OH/ROS	PET	Sulfate/chloride electrolytes	700 mV @10 mA cm^{-2}	100 (CO_2-based oxidation)	230	50 h @10 mA cm^{-2}	Commercial reagent PET MPs	[143]

4. Advances in Electrocatalytic Systems for PET Fiber Degradation

Advances in electrocatalytic systems for PET fiber degradation have revealed representative catalyst families that capture key mechanistic principles and practical potential [144]. However, it should be clarified that most of these advanced catalyst systems have been evaluated using model substrates such as ethylene glycol or PET hydrolysates, and only limited studies have validated their performance on actual textile or fiber waste, where structural complexity and surface modifications may significantly influence degradation behavior. It begins with metals and alloys, where elemental composition and alloying strategies influence redox flexibility, surface adsorption, and tolerance to contaminants. It then turns to metal oxides, a diverse class that includes spinels, perovskites, and conductive oxides, in which lattice oxygen activity, vacancy engineering, and semiconducting properties govern radical generation and stability. Metal hydroxides are considered next, particularly layered double hydroxides, which provide tunable interlayer chemistry and strong alkaline microenvironments that accelerate ester bond scission. The discussion proceeds to metal sulfides and phosphides, materials whose anion chemistry and electronic configurations make them efficient in persulfate or peroxymonosulfate activation while also enabling cathodic hydrogen-mediated processes. Finally, the section highlights emerging materials such as carbon-based frameworks, metal–organic frameworks, carbides, and nitrides, which offer new design spaces for high dispersion of active sites, adjustable conductivity, and robust interfacial architectures. By comparing these categories within a unified perspective, the section aims to identify how structural and electronic attributes of different electrocatalyst systems translate into performance, durability, and scalability for PET fiber degradation.

4.1. Metals and Alloys

Metals and alloys constitute one of the earliest and most versatile classes of electrocatalysts explored for PET fiber degradation, largely because their surface electronic structures and redox flexibility provide direct routes for activating both oxidative and reductive processes relevant to ester bond cleavage. Transition metals such as nickel, cobalt, copper, and iron exhibit variable oxidation states that allow them to participate in Fenton-like or anodic redox cycles, generating hydroxyl radicals or other high-valence intermediates capable of depolymerizing PET into monomers such as TPA and EG. At cathodic potentials, metals can adsorb hydrogen atoms (H*) and locally increase alkalinity, thereby promoting hydrolytic or alcoholytic pathways that are otherwise kinetically hindered in dense crystalline fibers. Alloys extend this functionality by creating synergistic electronic environments in which one element enhances conductivity or stabilizes high-valence centers while the other tunes adsorption energy for intermediates like BHET or oligomeric fragments. For instance, Ni–Fe and Co–Fe alloys demonstrate improved charge-transfer rates and enhanced radical flux compared to their monometallic counterparts, a result of modified d-band positions and stronger metal–metal interactions [145]. Furthermore, metallic surfaces can catalyze *in situ* activation of peroxymonosulfate or persulfate, generating sulfate radicals with higher selectivity for ester bond scission. Despite these advantages, metals and alloys also face critical challenges: dissolution, surface passivation, and susceptibility to interference from dyes or heavy metals present in real textile waste can compromise long-term stability [146,147]. Addressing these limitations requires strategies such as alloying to resist corrosion, coupling with conductive supports to mitigate leaching, or engineering surface oxides that act as protective yet active layers. Overall, metals and alloys illustrate how electronic structure engineering at the atomic scale directly impacts electrocatalytic PET fiber degradation, offering both mechanistic insight and a foundation for more advanced hybrid catalyst systems [148].

Building on the insights from metal and alloy catalysts, recent studies have focused on enhancing the catalytic performance by exploring advanced nanostructures and alloy compositions that offer better control over electronic properties and reaction kinetics. Sun et al. reported bimetallic PdCu mesoporous nanocavities as an electrocatalyst to enable concurrent nitrate reduction and PET-derived ethylene glycol oxidation [107]. The uniform nanocavity-rich morphology with open mesoporous channels is clearly revealed by SEM, indicating abundant confined yet accessible active regions for electrocatalysis (Figure 5a). High-resolution transmission electron microscope (TEM) further resolves well-defined alloy lattice fringes with a contracted interplanar spacing of ~0.22 nm, confirming successful Pd–Cu alloying and the presence of low-coordination surface sites associated with the curved nanocavity walls (Figure 5b). Electrochemical polarization curves show that PdCu nanocavities markedly lower the onset potential and enhance current density for ethylene glycol oxidation compared with the blank electrolyte, demonstrating facilitated alcohol oxidation kinetics induced by the alloyed metal surface (Figure 5c). Correspondingly, product analysis reveals high Faradaic efficiencies toward glycolic acid (GA) and formic acid (FA) over a wide potential window, highlighting the potential-regulated selectivity enabled by the PdCu alloy nanostructure (Figure 5d). Further advancing catalyst design, the incorporation of Pd into Co–Ni alloys has demonstrated enhanced surface reconstruction and electronic synergy, providing a pathway to fine-tune the reaction mechanisms and optimize the performance for PET-derived ethylene glycol oxidation. Further advancing catalyst design, the incorporation of Pd into Co–Ni alloys has demonstrated enhanced surface reconstruction and electronic synergy, providing a viable pathway to fine-tune reaction mechanisms and optimize the performance of PET-derived ethylene glycol oxidation. Fan et al. reported a Pd-doped Co–Ni catalyst to elucidate how dynamic surface reconstruction and metal–metal electronic coupling regulate ethylene glycol oxidation in tandem with hydrogen evolution [125]. The proposed reconstruction-assisted electrocatalytic process indicates that Pd incorporation accelerates EG adsorption and activation, while simultaneously facilitating rapid formate formation through optimized surface electronic states (Figure 5e). *In situ* structural analyses reveal the generation of surface nanoclusters and localized reconstruction under anodic polarization, suggesting that Pd plays a critical role in stabilizing dynamically formed active sites during continuous electrolysis (Figure 5f). Electrochemical evaluations further demonstrate a substantially reduced onset potential and enhanced current density for Pd–CoNi compared with undoped counterparts, confirming that Pd doping effectively improves charge-transfer kinetics via electronic synergy (Figure 5g). Correspondingly, markedly improved Faradaic efficiency and product productivity establish that reconstruction-driven electronic modulation directly translates into higher catalytic selectivity and overall efficiency (Figure 5h).

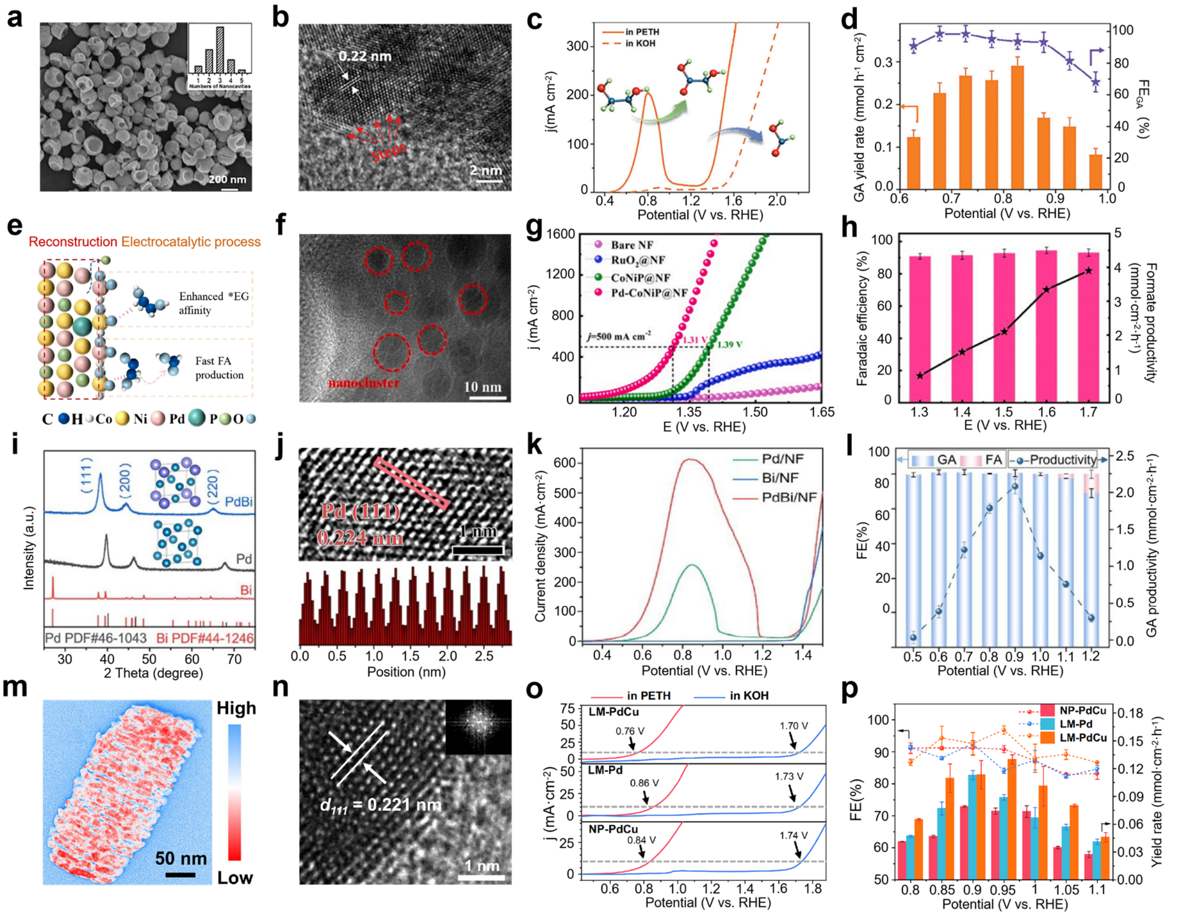

Figure 5. (**a**) SEM of PdCu MC Nanozymes,PdCu MC nanozymes with nanocavities (scale bar = 200 nm). (**b**) High-resolution TEM of PdCu MC Nanozymes, uniformly distributed nanocavities (50–100 nm, scale bar = 2 nm). (**c**) Current density vs. potential for ethylene glycol oxidation reactions (EGOR) in PETH and KOH electrolytes. Inset: EG oxidation reaction pathway. (**d**) Potential-dependent GA yield rates and Faradic efficiencies (FEs) for EG oxidation, highlighting PdCu MC performance. Reproduced with permission from Ref. [107]. Copyright 2024, John Wiley and Sons. (**e**) Schematic of the reconstruction electrochemical process, enhanced EG affinity and fast formate (FA) production, during the electrocatalytic process. (**f**) High-resolution TEM image of nanoclusters formed on the Pd-CoNiP@NF electrode surface, scale bar of 10 nm. (**g**) Linear sweep voltammetry (LSV) curves for EG oxidation (EGOR) of Pd-CoNiP@NF, RuO_2@NF, CoNiP@NF and bare NF electrodes in 1 M KOH + 0.12 M EG; inset of Tafel plots comparison for these electrodes. (**h**) Potential-dependent Faradaic efficiency and formate productivity of Pd-CoNiP@NF electrode during EG oxidation in 1 M KOH + 0.12 M EG, high catalytic performance of the electrode. Reproduced with permission from Ref. [125]. Copyright 2025, Elsevier. (**i**) XRD patterns of Pd, Bi, and PdBi alloys, characteristic peaks at (111), (200), and (220) diffraction planes, confirmation

of alloy formation. (**j**) High-resolution TEM image of PdBi alloy, (111) lattice fringe with a spacing of 0.224 nm, confirmation of the crystalline structure. (**k**) LSV curves of Pd/NF, Bi/NF, and PdBi/NF in PET hydrolysate (0.5 M EG), enhanced electrocatalytic activity of PdBi/NF. (**l**) Faradaic efficiency and glycolic acid productivity of PdBi/NF at different potentials, high GA selectivity and productivity of the electrode. Reproduced with permission from Ref. [110]. Copyright 2025, John Wiley and Sons. (**m**) TEM image of LM-PdCu, lamellar mesoporous structure, scale bar of 50 nm, stacked morphology. (**n**) High-resolution TEM image, lattice fringes of Pd (111) with a d-spacing of 0.221 nm, confirmation of the crystalline structure. (**O**) LSV curves of LM-PdCu, LM-Pd, and NP-PdCu in 1 M KOH and PETH, reduced potential for EG oxidation in PETH. (**p**) Faradaic efficiency and yield rate of glycolic acid of NP-PdCu, LM-Pd, and LM-PdCu at different potentials, superior performance in GA electrosynthesis. Reproduced with permission from Ref. [111]. Copyright 2024, Springer Nature.

Building on the dynamic surface reconstruction observed in Pd–CoNi catalysts, the introduction of Bi into PdBi alloys further refines the electronic structure, enabling more selective oxidation pathways and enhancing the overall catalytic efficiency for PET upcycling. Kang et al. investigated a PdBi alloy anode for the selective electrooxidation of PET-derived EG to glycolic acid [110]. Structural characterization confirms the formation of a well-alloyed PdBi phase, where systematic diffraction peak shifts relative to metallic Pd indicate successful incorporation of Bi into the Pd lattice rather than physical mixing (Figure 5i). High-resolution TEM further reveals expanded lattice fringes within PdBi crystalline domains, providing direct evidence that Bi alloying induces geometric distortion of Pd active ensembles (Figure 5j). Electrochemical evaluations demonstrate that PdBi exhibits a higher oxidation current density and a lower onset potential for ethylene glycol oxidation compared with monometallic Pd, reflecting accelerated reaction kinetics enabled by alloy-induced electronic modulation (Figure 5k). Correspondingly, the PdBi catalyst delivers near-unity Faradaic efficiency toward glycolic acid over a broad potential window, indicating that Bi incorporation effectively suppresses over-oxidation pathways and stabilizes glycolic acid as the dominant product (Figure 5l). Han et al. reported a lamellar mesoporous PdCu alloy (LM-PdCu) as a highly efficient electrocatalyst for polyethylene terephthalate (PET) upcycling to glycolic acid [111]. The low-magnification TEM images show that LM-PdCu consists of uniformly dispersed, one-dimensional stacked nanostructures with well-defined lamellar morphology, indicating successful construction of ordered mesoporous metal frameworks (Figure 5m). High-resolution TEM further reveals clear lattice fringes with an interplanar spacing of ~0.221 nm, corresponding to the (111) plane of face-centered cubic PdCu alloy, confirming the formation of a well-alloyed metallic phase (Figure 5n). Electrochemical polarization curves demonstrate that LM-PdCu exhibits significantly lower onset potentials for PET-derived ethylene glycol oxidation compared with pure Pd and nanoparticle PdCu, reflecting enhanced intrinsic activity induced by alloying and mesoporous architecture (Figure 5o). Meanwhile, Faradaic efficiency and product distribution analysis show that LM-PdCu achieves high selectivity toward glycolic acid over a wide potential window, accompanied by an increased yield rate relative to control catalysts (Figure 5p).

4.2. Metal Oxides

Metal oxides have emerged as a central class of electrocatalysts for PET fiber degradation because their crystal lattices and variable valence states provide highly tunable platforms for generating reactive oxygen species and stabilizing intermediates during ester bond scission. Oxides such as RuO_2, MnO_2, and spinel or perovskite-type structures are particularly effective under anodic polarization, where lattice oxygen and surface hydroxyl groups participate in high-valence redox cycles that yield ·OH and related oxidants at the electrode–fiber interface. The density of oxygen vacancies and the mobility of lattice oxygen are key descriptors: higher vacancy concentrations increase the rate of radical formation and facilitate charge transfer, while lattice oxygen redox activity can directly contribute to breaking C–O bonds in the PET backbone. Moreover, oxide semiconductors form space charge layers that influence electron–hole separation, thereby modulating oxidant flux and improving the selectivity of ester cleavage over uncontrolled aromatic oxidation [149]. For example, PbO_2 and SnO_2-based electrodes can sustain high overpotentials without rapid deactivation, enabling continuous radical production, whereas MnO_x or Co_3O_4 spinels exploit mixed valence states to catalyze both hydroxyl radical generation and peroxymonosulfate activation. Beyond intrinsic activity, oxides also provide chemical stability against corrosive electrolytes and structural rigidity needed for repeated cycling [150]. However, challenges remain in achieving sufficient conductivity, preventing surface passivation, and suppressing nonselective mineralization of aromatic rings [151]. To overcome these issues, strategies such as doping with heteroatoms to adjust band positions, constructing heterojunctions with carbon or metals to accelerate electron transport, and engineering nanostructured morphologies to maximize interfacial contact with PET fibers have been employed. Collectively, metal oxides demonstrate how crystallographic design, defect engineering, and electronic modulation can converge to deliver catalysts that couple robust stability with targeted depolymerization activity in the degradation of PET fibers.

In addition to the fundamental insights provided by metal oxides, recent studies have explored the use of mixed metal oxide anodes, which further enhance catalytic efficiency by facilitating indirect oxidation pathways and improving the overall degradation process. Mais et al. investigated the direct electrochemical degradation of PET using mixed metal oxide anodes, emphasizing indirect oxidation pathways mediated by reactive chlorine species [106]. Scanning electron microscopy images show that PET particles develop roughened and fragmented surfaces after electrochemical treatment, indicating that degradation proceeds through surface-confined oxidative attack rather than bulk structural collapse (Figure 6a). Time-resolved ATR–FTIR spectra reveal the gradual attenuation of characteristic ester-related vibrational bands, confirming progressive cleavage of PET ester linkages during electrolysis without accumulation of stable intermediate functionalities (Figure 6b).The periodic variation in chloride concentration during long-term operation demonstrates sustained generation and consumption of active chlorine species, establishing indirect oxidation as the dominant mechanism governing PET depolymerization on mixed metal oxide electrodes (Figure 6c). Expanding on the use of mixed metal oxide electrodes, recent advancements in electrode reconstruction, such as the electro-reconstruction of NiCo nanosheets, have shown significant improvements in reaction kinetics and selectivity, further enhancing the efficiency of PET-derived ethylene glycol oxidation. Wang et al. electro-reconstructed a NiCo nanosheet electrode on Ni foam (R-NiCo/NF) to promote selective oxidation of PET-derived EG (coupled with nitrate reduction) [105]. The phase evolution from hydroxides to oxyhydroxides is evidenced by the disappearance of $Ni(OH)_2/Co(OH)_2$ features and the emergence of NiOOH/CoOOH signatures after reconstruction, indicating formation of the redox-active Ni^{3+}/Co^{3+} centers required for anodic alcohol oxidation (Figure 6d). Consistently, the lattice-resolved microscopy identifies characteristic spacings assignable to CoOOH and NiOOH planes, confirming that the reconstructed surface is dominated by catalytically competent oxyhydroxide domains rather than the initial deposited phase (Figure 6e). Building on these structural fingerprints, polarization analysis shows that the reconstructed NiCo anode can sustain high anodic currents for EG oxidation, enabling high Faradaic efficiency toward formate in the coupled system. This behavior reflects a coherent structure–activity relationship in which *in situ* reconstruction leads to active oxyhydroxide formation and, consequently, enhanced EGOR performance (Figure 6f).

Similarly, the study of spinel oxides like $MnCo_2O_4$ and $CoCo_2O_4$ underscores the importance of lattice oxygen activity in tuning catalytic behavior, with distinct differences in the formation and selectivity of formate during electrochemical oxidation of PET-derived EG. Chen et al. monitored PET-derived ethylene glycol oxidation on a model spinel series (MCo_2O_4) and used operando spectroscopy to directly compare how fast formate signatures emerge on different lattices [96]. TEM analysis reveals that $NiCo_2O_4$ consists of uniformly distributed nanocrystalline particles with a polycrystalline spinel structure, as confirmed by the SAED pattern indexed to the (311) and (400) planes (Figure 6g). HRTEM further resolves clear lattice fringes with interplanar spacings of 0.460, 0.244, and 0.203 nm, corresponding to the (111), (311), and (400) crystal planes of $NiCo_2O_4$, respectively, demonstrating its high crystallinity and well-defined spinel lattice (Figure 6h). An economic assessment of different MCo_2O_4 catalysts shows that $MnCo_2O_4$, $FeCo_2O_4$, and $FeCo_2O_4$ generate cumulative net losses of −198, −278, and −386 \$ ton^{-1}, respectively, whereas $CuCo_2O_4$ and $NiCo_2O_4$ achieve positive net profits of 269 and 739 \$ ton^{-1}, with $NiCo_2O_4$ delivering the highest economic return among the investigated catalysts, highlighting its strong potential for economically viable PET upcycling (Figure 6i). Building on the insights from spinel oxides, the incorporation of oxygen vacancies into Fe-doped Nb_2O_5 further refines the electronic structure, enabling more efficient ethylene glycol oxidation and enhancing the catalytic performance for PET upcycling. Qi et al. investigated Fe-doped Nb_2O_5 as an oxygen-vacancy-rich oxide support to regulate Pd electronic structure and promote ethylene glycol electro-oxidation [97]. The electron density difference analysis reveals pronounced interfacial charge redistribution between Pd nanoparticles and Fe-doped Nb_2O_5, indicating electron transfer from Pd to the vacancy-rich oxide surface and the formation of a Pd–O–Nb electronic coupling pathway (Figure 6j).High-resolution TEM images show locally distorted lattice fringes and defect-rich regions within Fe-doped Nb_2O_5, confirming that Fe incorporation induces oxygen vacancies and lattice disorder while maintaining structural integrity (Figure 6k). Electron paramagnetic resonance spectra display an intensified signal at $g \approx 2.004$ after Fe doping, directly evidencing the increased concentration of oxygen vacancies that act as electronic mediators for Pd–support interaction (Figure 6l).

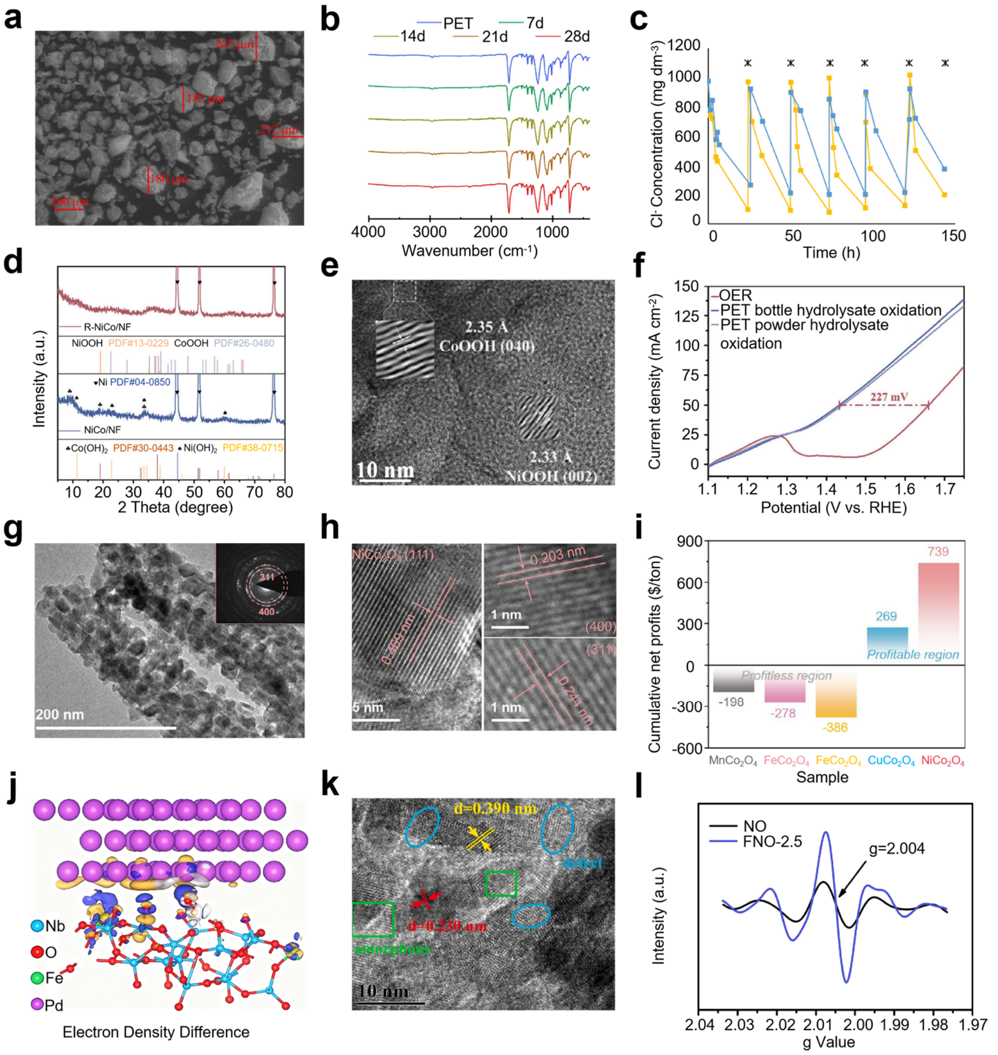

Figure 6. (**a**) Low-magnification SEM of PE microplastics, particle sizes ranging from 150 μm to 200 μm. (**b**) FTIR spectra of PET at different time points (14, 21, and 28 days), structural changes of PET. (**c**) Chloride concentration changes over time during electrolysis at 10 and 20 mA cm^{-2}. Reproduced with permission from Ref. [106]. Copyright 2024, Royal Society of Chemistry. (**d**) LSV curves of R-Co/CF in simulated wastewater with and without 0.1 M NO_3^-, electrocatalytic performance of R-Co/CF for nitrate reduction. (**e**) Faradaic efficiency, selectivity, and production rate of NH_3 in simulated chemical and natural wastewater with R-Co/CF. (**f**) LSV curves of R-NiCo/NF in PET hydrolysate and KOH, catalytic activity of R-NiCo/NF for PET hydrolysate oxidation. Reproduced with permission from Ref. [105]. Copyright 2025, John Wiley and Sons. (**g**) TEM image of $NiCo_2O_4$ nanoneedles with lattice fringes, inset of selected area electron diffraction (SAED) pattern. (**h**) High-resolution TEM image of $NiCo_2O_4$, interplanar distances of 0.203 nm and 0.244 nm for the (111) and (400) planes. (**i**) Comparison of Faraday efficiencies for formate and hydrogen production with $NiCo_2O_4$ as catalyst, high selectivity and efficiency of $NiCo_2O_4$. Reproduced with permission from Ref. [96]. Copyright 2025, John Wiley and Sons. (**j**) Electron density difference plot of Pd/FNO-2.5 catalyst, electron enrichment and depletion, interaction between Pd and Fe-doped Nb_2O_5. (**k**) High-resolution TEM image of Pd/FNO-2.5, lattice fringes with interplanar distances for (111) plane of Pd and (001) plane of FNO-2.5, respectively. (**l**) EPR spectra of Pd/FNO-2.5, distinct g-value at 2.004, oxygen vacancies and unpaired electrons in the Fe-doped Nb_2O_5 structure. Reproduced with permission from Ref. [97]. Copyright 2023, Elsevier.

4.3. Metal Hydroxides

Metal hydroxides, particularly transition metal hydroxides and layered double hydroxides (LDHs), have attracted significant attention as electrocatalysts for PET fiber degradation because their lamellar structures and tunable surface chemistry create favorable microenvironments for selective ester bond cleavage. Unlike oxides that rely mainly on lattice oxygen activity, hydroxides possess abundant hydroxyl groups and interlayer anions that participate directly in redox cycling and radical generation. Under anodic polarization, metal hydroxides such as $Ni(OH)_2$, $Co(OH)_2$, and $Fe(OH)_3$ undergo valence transitions to high-valence species (e.g., Ni^{3+}, Co^{3+}, Fe^{3+}), which can activate water or persulfate to produce··OH and SO_4^- radicals, thereby promoting oxidative depolymerization of PET. LDHs further extend this functionality by enabling cation substitution and interlayer anion exchange, which adjust electronic structure, improve conductivity, and enhance adsorption of PET-derived oligomers or intermediate products such as BHET. Their alkaline character also creates localized high-pH environments at the fiber–electrolyte interface, which facilitates hydrolysis of ester bonds and synergistically accelerates electro-oxidation. Moreover, the high surface area and porous nanosheet morphology of hydroxides promote strong electrolyte infiltration and maximize three-phase boundary contact with PET fibers, overcoming some of the mass transport barriers imposed by fiber crystallinity and surface coatings. Despite these advantages, metal hydroxides suffer from moderate electrical conductivity and can undergo structural reconstruction or dissolution during long-term cycling, which reduces stability. To address these issues, hybrid designs that integrate hydroxides with conductive substrates (carbon cloth, graphene, MXenes) or form heterostructures with oxides and metals are being actively explored to improve charge transport and durability. Overall, the distinctive lamellar structure, tunable redox chemistry, and alkaline interface of metal hydroxides make them uniquely suited to couple hydrolytic and oxidative pathways, positioning them as promising electrocatalysts for efficient and selective degradation of PET fibers.

To further enhance the catalytic efficiency of metal hydroxides, recent studies have incorporated heterostructured designs, such as Pd@$Ni(OH)_2$–NiO, which enable improved electronic regulation and offer greater selectivity for PET-derived ethylene glycol oxidation. Li et al. reported a Pd@$Ni(OH)_2$–NiO heterostructured catalyst designed to enhance electrocatalytic oxidation of PET-derived EG through interfacial electronic regulation and phase cooperation [119]. The schematic structural model illustrates that metallic Pd nanoparticles are selectively anchored on $Ni(OH)_2$–NiO domains, forming abundant metal–hydroxide interfaces that are expected to promote charge redistribution and facilitate reactant activation during EG oxidation (Figure 7a). High-resolution TEM reveals clear lattice fringes corresponding to Pd, $Ni(OH)_2$, and NiO phases, confirming the successful construction of a multi-phase heterointerface rather than a physical mixture, which is critical for interfacial synergistic catalysis (Figure 7b). Electrochemical polarization curves demonstrate distinct anodic features associated with reversible OH* adsorption/desorption on $Ni(OH)_2$, indicating that the hydroxide matrix actively participates in surface redox chemistry during EG oxidation (Figure 7c). Product analysis shows high Faradaic efficiency toward formic acid and glycolic acid over a wide potential window, confirming that Pd-induced electronic modulation of $Ni(OH)_2$–NiO suppresses over-oxidation and steers selective C–C bond cleavage pathways (Figure 7d). In addition to heterostructured catalysts, doping with transition metals, such as Mn in $Ni(OH)_2$, further refines the electronic properties, enhancing both the catalytic activity and product selectivity during ethylene glycol oxidation. Wang et al. systematically investigated Mn-doped $Ni(OH)_2$ as a model metal hydroxide catalyst to elucidate how electronic structure modulation governs product selectivity during ethylene glycol electro-oxidation [120]. The electronic structure schematic illustrates that Mn incorporation into the $Ni(OH)_2$ lattice induces eg-band broadening and modifies the local electronic density near the Fermi level, which is expected to regulate EG adsorption and suppress over-oxidation pathways (Figure 7e). The atomic structural model further shows that Mn substitution introduces lattice distortion within the layered hydroxide framework, providing electronically heterogeneous Ni active sites while maintaining the overall lamellar structure (Figure 7f). Linear sweep voltammetry reveals that Mn–$Ni(OH)_2$ delivers a higher anodic current density for EG oxidation than pristine $Ni(OH)_2$, indicating accelerated reaction kinetics induced by optimized electronic states (Figure 7g). Correspondingly, product distribution analysis demonstrates significantly enhanced formate selectivity together with high Faradaic efficiency, confirming that Mn-induced electronic modulation effectively steers the reaction pathway toward selective C–C bond cleavage rather than deep oxidation (Figure 7h).

Building on the benefits of doping strategies, the incorporation of additional metal ions, such as Co and V in layered double hydroxides, further optimizes electronic structure and enhances the catalytic efficiency for selective oxidation and hydrogen evolution during ethylene glycol oxidation. Lu et al. reported a Co–V layered double hydroxide (Co–V LDH) catalyst to couple PET-derived ethylene glycol oxidation with hydrogen evolution through lattice-level electronic modulation [121]. High-resolution TEM images reveal a well-defined layered morphology with clear lattice fringes, confirming the successful construction of a Co–V LDH structure that exposes abundant edge sites and interlayer channels for reactant access (Figure 7i). *In situ* infrared spectroscopy captures the potential-dependent emergence of surface-bound *CHO and *COO⁻ intermediates during ethylene glycol oxidation, indicating that Co–V LDH stabilizes key reaction intermediates and promotes stepwise C–C bond cleavage (Figure 7j). Electrochemical polarization curves show that Co–V LDH delivers a significantly higher anodic current density in PET hydrolysate compared with blank electrolyte, demonstrating that the layered hydroxide actively catalyzes EG oxidation rather than background oxygen evolution (Figure 7k). Faradaic efficiency analysis confirms high selectivity toward formic acid accompanied by sustained hydrogen production at the cathode, highlighting the dual-functional role of Co–V LDH in synchronizing selective EG oxidation and HER (Figure 7l). Further advancing these strategies, the integration of $Ni(OH)_2$ with MnO on a conductive Ni aerogel creates a highly efficient heterostructure that not only enhances ethylene glycol oxidation but also promotes hydrogen evolution, illustrating the potential of interfacial synergy in catalyst design. Fang et al. reported a $Ni(OH)\backslash_2$/MnO@Ni aerogel (NiMn AG) heterostructure to enhance EGOR-assisted hydrogen production via interfacial regulation [122]. The material design couples amorphous $Ni(OH)_2$ with MnO on a conductive Ni aerogel, creating abundant heterointerfaces that promote electron redistribution and optimize adsorption of EG oxidation intermediates (Figure 7m). Structural characterization confirms the coexistence of MnO and amorphous $Ni(OH)\backslash_2$ within the aerogel framework, indicating successful heterostructure formation rather than a physical mixture (Figure 7n). Electrochemical measurements show that NiMn AG delivers a markedly reduced EGOR overpotential (120 mV at 10 mA cm^{-2}) and faster kinetics compared with Ni AG, MnO, and RuO_2, highlighting the decisive role of interfacial synergy (Figure 7o). Product and energy analyses further demonstrate a low EGOR onset potential and high formate selectivity (~96%), validating that the $Ni(OH)\backslash_2$/MnO interface not only accelerates EG oxidation but also steers it toward value-added formate formation (Figure 7p).

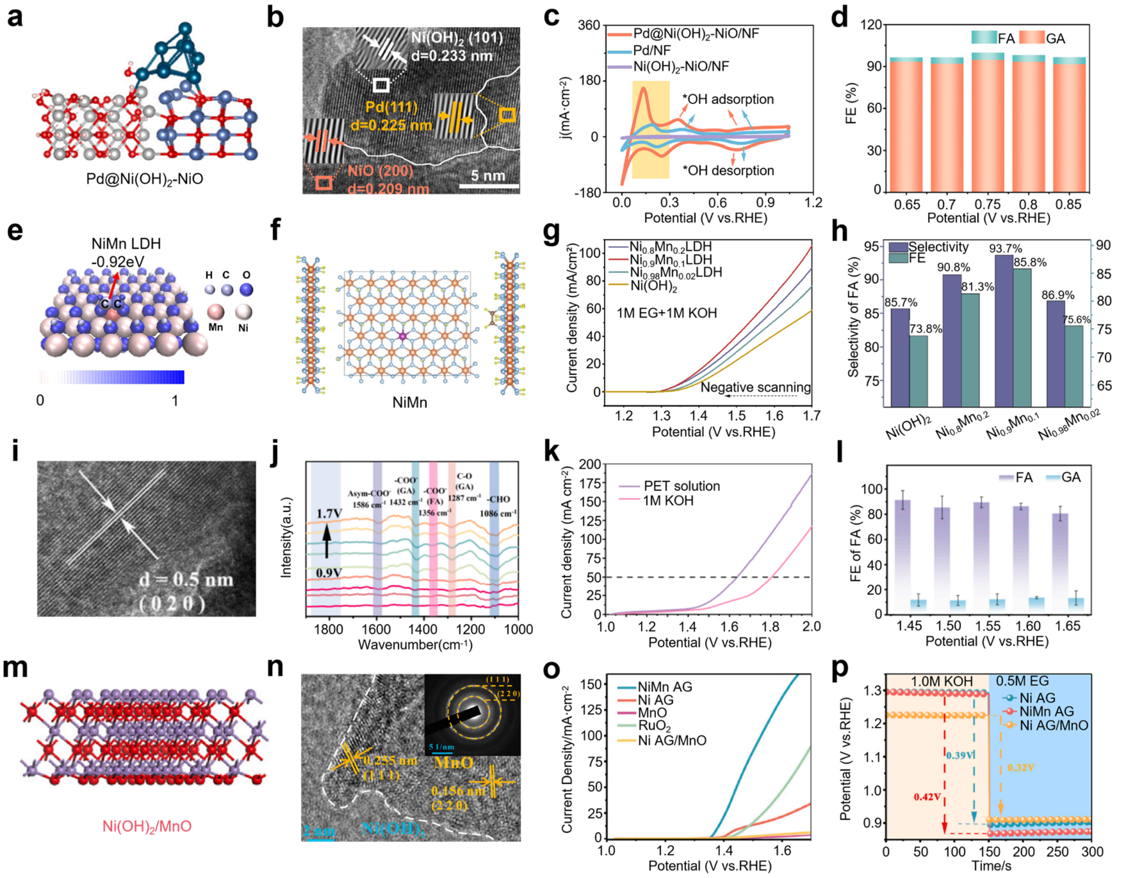

Figure 7. (**a**) Schematic representation of $Pd@Ni(OH)_2$-NiO with Pd supported by $Ni(OH)_2$-NiO. (**b**) TEM image of $Pd@Ni(OH)_2$-NiO, labeled interplanar distances of Pd(111) and NiO(200) planes. (**c**) Polarization curves of $Pd@Ni(OH)_2$-NiO, Pd, and $Ni(OH)_2$-NiO catalysts for ethylene glycol oxidation, catalytic performance comparison. (**d**) Faradic efficiency of glycolic acid and formic acid at different potentials during EGOR. Reproduced with permission from Ref. [119]. Copyright 2025, Elsevier. (**e**) Schematic of NiMn LDH, corresponding electronic states. (**f**) Layered structure of NiMn in NiMn LDH, metal oxide bonding. (**g**) Polarization curves of NiMn LDH catalysts and $Ni(OH)_2$ in 1 M EG and 1 M KOH, catalytic performance comparison. (**h**) Bar chart of different NiMn LDH catalysts, selectivity and Faradic efficiency comparison for formate production. Reproduced with permission from Ref. [120]. Copyright 2024, John Wiley and Sons. (**i**) High-resolution TEM of $NiCo_2O_4$, lattice fringes with a distance of 0.5 nm, correspondence to the (020) plane. (**j**) FTIR spectra during electrochemical reactions, characteristic peaks for formic acid and glycolic acid at different potentials (1.7 V and 0.9 V). (**k**) Current density vs. potential curves of $NiCo_2O_4$ in PET solution and 1 M KOH, electrocatalytic performance of $NiCo_2O_4$. (**l**) Faradic efficiency for formic acid and glycolic acid production at different potentials during the electrochemical reaction. Reproduced with permission from Ref. [121]. Copyright 2025, Elsevier. (**m**)

Schematic representation of $Ni(OH)_2/MnO$ heterostructure, Mn and Ni atoms. (**n**) TEM image of NiMn AG, lattice fringes and interplanar distances, highlighted planes for MnO and NiO. (**o**) Polarization curves of NiMn AG, Ni AG, MnO, RuO_2, and Ni AG/MnO in 1 M KOH and 0.5 M EG. (**p**) Chronoamperometry and Faradic efficiency (FE) tests of NiMn AG at different potentials during EGOR in KOH and EG. Reproduced with permission from Ref. [122]. Copyright 2024, Elsevier.

4.4. Metal Sulfides and Phosphides

Metal sulfides and phosphides thus emerge as a distinct class of electrocatalysts for PET fiber degradation, offering electronic structures and surface chemistries fundamentally different from those of conventional oxides and hydroxides. The incorporation of sulfur or phosphorus into transition metal lattices (e.g., NiS, CoS, MoS_2, Ni_2P, CoP) lowers the electronegativity contrast between metal and nonmetal atoms, resulting in enhanced covalency, higher electrical conductivity, and tunable d-band centers that promote efficient charge transfer during electrochemical processes. These features facilitate both anodic and cathodic pathways relevant to PET degradation. On the oxidative side, sulfides and phosphides can catalyze the activation of peroxymonosulfate (PMS) or persulfate, generating sulfate radicals (SO_4^-) and hydroxyl radicals (·OH) with strong oxidizing power to cleave ester bonds and depolymerize PET into monomers such as TPA and EG. On the reductive side, their ability to adsorb hydrogen intermediates (H*) and promote local alkalinity at cathodic potentials accelerates hydrolytic scission and alcoholysis reactions, which are otherwise kinetically hindered in crystalline fiber domains. Furthermore, the structural diversity of sulfides and phosphides, including layered structures (MoS_2) and nanophase alloys (Ni_2P/CoP composites), allows engineering of abundant edge sites, vacancies, and heterointerfaces that increase the density of active centers and provide pathways for selective adsorption of PET oligomers or BHET intermediates. Despite these advantages, stability remains a key concern: sulfides are prone to surface oxidation and leaching under anodic conditions, while phosphides may undergo gradual transformation into oxide or hydroxide phases during extended cycling, which can either diminish or, in some cases, dynamically enhance catalytic activity. To improve durability and selectivity, strategies such as encapsulation with conductive carbon shells, construction of core–shell heterostructures, and hybridization with oxides or nitrides have been proposed. Overall, metal sulfides and phosphides expand the design landscape for PET fiber electrocatalysis by coupling high conductivity, radical-mediated oxidation, and hydrogen-assisted hydrolysis,where conductive carbide- or phosphide-related backbones offer structural robustness under electrochemical conditions, offering versatile platforms for developing next-generation systems tailored to the challenges of fiber degradation.

Building on the advantages of metal sulfides and phosphides, recent research has focused on developing nanosheet and heterostructured catalysts, which further enhance the catalytic performance for PET-derived ethylene glycol oxidation by optimizing the reaction pathways and product selectivity. Ma et al. investigated Ni–Co–S nanosheet arrays (Ni–Co_9S_8 NSAs) grown on Ni foam as an anodic catalyst for PET-derived EG oxidation to formate, aiming to couple efficient EGOR with hydrogen evolution [135]. The nanosheet array morphology uniformly covers the Ni foam skeleton, providing a hierarchical and porous architecture that maximizes exposed active sites and facilitates mass/electron transport during EG oxidation (Figure 8a). High-resolution structural analysis reveals well-defined lattice fringes corresponding to Co_9S_8 crystal planes, confirming successful sulfurization and the formation of crystalline Ni–Co sulfide domains within the nanosheets (Figure 8b). Electrochemical polarization curves demonstrate that Ni–Co_9S_8 NSAs/NF exhibit a markedly reduced EGOR onset potential and higher current density compared with Ni foam and Co-MOF-derived references, indicating accelerated EG oxidation kinetics (Figure 8c). Product distribution analysis shows dominant formate formation with Faradaic efficiencies exceeding ~90%, validating that the Ni–Co–S catalyst selectively channels PET-derived EG toward value-added formate rather than over-oxidation pathways (Figure 8d). Further advancing these catalytic strategies, the incorporation of transition metals such as Ni in cobalt phosphide catalysts, particularly in ordered macroporous structures, enhances both the reaction kinetics and the selectivity of ethylene glycol oxidation, offering a new pathway for efficient PET upcycling. Wang et al. developed an ordered macroporous Ni-modified cobalt phosphide (OMS-Ni_1-CoP) electrocatalyst to enable efficient EGOR-assisted hydrogen production through structural and electronic regulation [126]. The high-resolution TEM image reveals that the OMS-Ni_1-CoP framework consists of uniformly distributed CoP nanocrystallites with clear lattice fringes, confirming the formation of crystalline phosphide domains within the macroporous skeleton (Figure 8e). Electrochemical polarization curves demonstrate that OMS-Ni_1-CoP exhibits a significantly reduced overpotential for EGOR compared with undoped CoP and control samples, indicating accelerated oxidation kinetics induced by Ni modification and hierarchical porosity (Figure 8f). Comparative current density plots further show that OMS-Ni_1-CoP outperforms reference catalysts such as RuO_2 and Ni_1-CoP, highlighting the synergistic effect between atomic-scale Ni incorporation and the ordered macroporous architecture (Figure 8g). Product analysis confirms a high Faradaic efficiency for formate formation over a broad potential window, verifying that the reconstructed phosphide-derived oxyhydroxide surface selectively promotes C–C bond cleavage toward value-added formate rather than complete mineralization (Figure 8h).

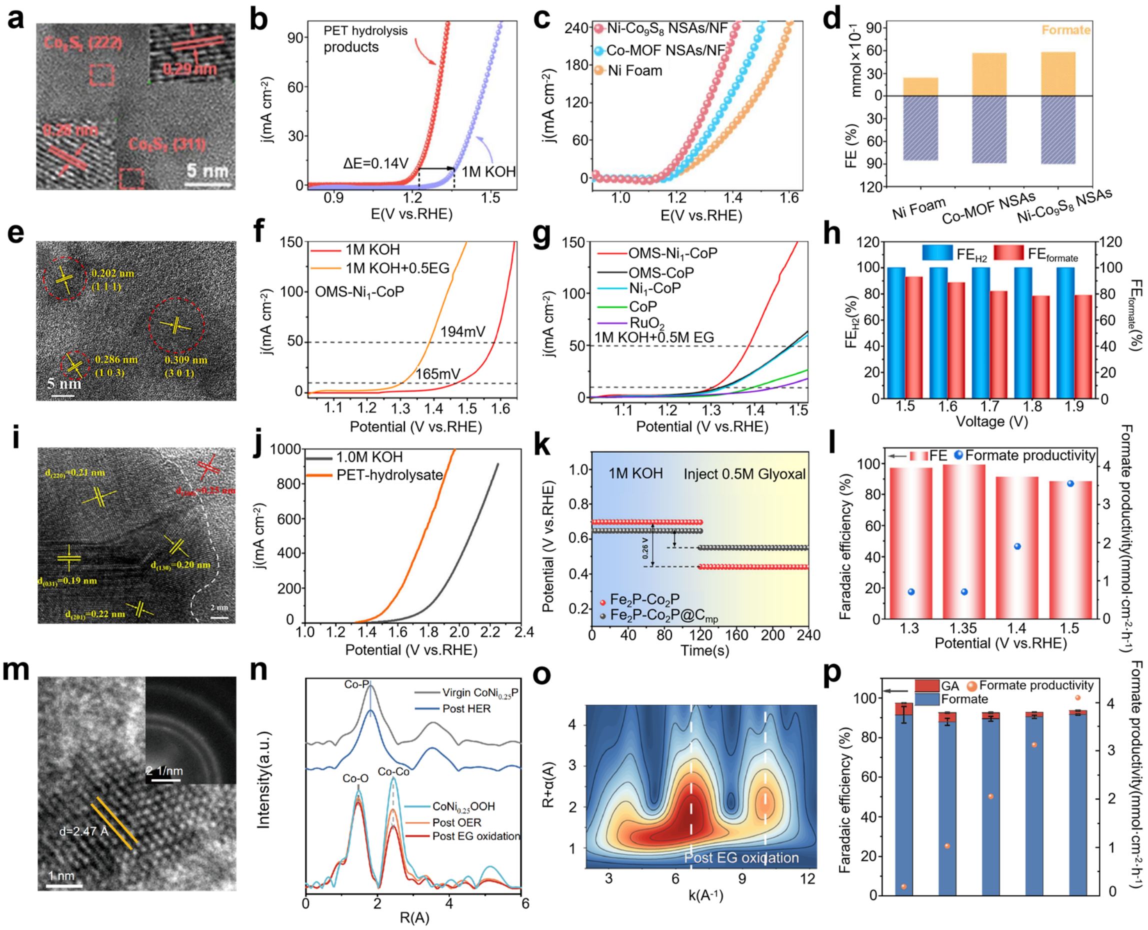

Figure 8. (**a**) High-resolution TEM image of Co_3S_8 NSAs, interplanar distance of 0.29 nm indexed to the (222) plane. (**b**) Polarization curves of PET hydrolysis products in 1 M KOH, reaction efficiency comparison with potential difference (ΔE) at 1.2 V and 1.5 V. (**c**) Current density vs. potential curves of Co-MOF NSAs/NF, Ni foam, and Ni-CoS_8 NSAs/NF during ethylene glycol oxidation reactions. (**d**) Faradic efficiency (FE) for formate (FA) production, catalytic performance of Ni foam, Co-MOF NSAs, and Ni-CoS_8 NSAs/NF at various potentials. Reproduced with permission from Ref. [135]. Copyright 2024, Royal Society of Chemistry. (**e**) High-resolution TEM image of OMS-Ni_1-CoP, well-defined atomic structures with mesopores (yellow arrows) distributed across the nanoparticle walls. (**f**) LSV curves of OMS-Ni_1-CoP in 1 M KOH (red) and 1 M KOH + 0.5 M EG (orange), sharp increase in current density for EGOR at lower potential compared to OER. (**g**) Comparison of LSV curves for OMS-Ni_1-CoP (red) and other catalysts (Ni_1-CoP, CoP, RuO_2), improved catalytic performance in 1 M KOH + 0.5 M EG for EGOR. (**h**) Faradaic efficiency for formic acid and glycolic acid production over OMS-Ni_1-CoP, high selectivity for formate at varying potentials. Reproduced with permission from Ref. [126]. Copyright 2022, Elsevier. (**i**) TEM image of Fe_2P-Co_2P catalyst, interplanar distances of 0.19–0.22 nm, well-formed crystalline phases. (**j**) LSV curves of Fe_2P–Co_2P in 1 M KOH (black) and PET hydrolysate (orange), onset potential shift for EGOR. (**k**) Stability test of Fe_2P–Co_2P in 1 M KOH electrolyte with 0.5 M Glyoxal, potential shift during continuous electrolysis. (**l**) Faradic efficiency (FE) for formate (FA) production with Fe_2P–Co_2P catalyst, high FE for formate production across different potentials. Reproduced with permission from Ref. [127]. Copyright 2025, John Wiley and Sons. (**m**) High-resolution TEM image of $CoNi_{0.25}P$ catalyst, interplanar distances of 0.19–0.22 nm, clear lattice fringes indexed to specific crystal planes. (**n**) X-ray absorption fine structure (XAFS) spectra of $CoNi_{0.25}P$ catalyst before and after different reactions (HER, OER, EG oxidation), spectral evolution. (**o**) Kinetic data of $CoNi_{0.25}P$ in EG oxidation, catalytic activity, clear evidence of active site evolution during the reaction process. (**p**) Faradic efficiency and formate productivity analysis at different potentials, high selectivity (>80%) for formate production. Reproduced with permission from Ref. [128]. Copyright 2021, Springer Nature.

In a similar vein, the integration of bio-derived mesoporous carbon with phosphide catalysts, such as Fe_2P–Co_2P@Cmp, offers further improvements in catalytic performance, enhancing both the efficiency and selectivity of ethylene glycol oxidation through structural optimization and surface reconstruction. Xia et al. reported a yeast-derived Fe_2P–Co_2P@mesoporous carbon (Fe_2P–Co_2P@Cmp) catalyst to achieve highly selective EGOR-assisted hydrogen production via surface reconstruction and intermediate confinement (Figure 8i) [127]. Linear sweep voltammetry demonstrates that the PET hydrolysate electrolyte delivers substantially higher oxidation currents and a lower reaction onset potential than the blank 1.0 M KOH electrolyte, confirming the favorable electrocatalytic oxidation kinetics of PET-derived ethylene glycol on the reconstructed phosphide catalyst (Figure 8j). Electrochemical polarization curves show that Fe_2P–Co_2P@Cmp significantly lowers the EGOR onset potential and delivers higher current densities than bare phosphides, highlighting the synergistic effect of Fe–Co coupling and the mesoporous carbon confinement (Figure 8k). Product analysis further confirms an ultrahigh Faradaic efficiency for formic acid formation (up to 99.1%), validating that the reconstructed phosphide-derived oxyhydroxide surface effectively promotes C–C bond cleavage while suppressing side reactions (Figure 8l). Building on these advancements, the dynamic surface reconstruction observed in Ni-modified cobalt phosphide catalysts, such as $CoNi_{0.25}P$, further accelerates ethylene glycol oxidation and hydrogen evolution, showcasing the significant impact of tailored structural and electronic properties on catalytic efficiency. Zhou et al. reported a Ni-modified cobalt phosphide ($CoNi_{0.25}P$) electrocatalyst that enables high-rate EG oxidation to formate coupled with hydrogen evolution through dynamic surface reconstruction [128]. The atomic-scale structural model illustrates that partial Ni incorporation into the CoP lattice induces electronic modulation and facilitates the formation of a reconstructed oxy(hydroxide) active phase under anodic conditions (Figure 8m). High-resolution TEM and diffraction analyses reveal that the pristine $CoNi_{0.25}P$ undergoes *in situ* transformation into a low-crystallinity Co–Ni oxy(hydroxide) while retaining structural integrity during operation (Figure 8n). Electrochemical polarization curves demonstrate that $CoNi_{0.25}P$ achieves exceptionally high current densities for EG oxidation with substantially reduced overpotential compared with benchmark catalysts, indicating accelerated C–C bond cleavage kinetics (Figure 8o). Product distribution and Faradaic efficiency analyses confirm dominant formate production (>80% FE) over a wide potential window, validating that the reconstructed oxy(hydroxide) surface selectively drives EG oxidation toward value-added formate rather than overoxidation pathways (Figure 8p).

4.5. Other Emerging Materials

Beyond conventional inorganic electrocatalysts, a growing class of emerging materials has opened new conceptual pathways for PET degradation and upcycling by redefining how electron transfer, bond activation, and reaction selectivity are controlled at the molecular and atomic levels [152,153]. Electro-organocatalytic systems exemplify this shift by replacing lattice-mediated redox chemistry with single-electron transfer processes, in which electrochemically generated organic redox mediators directly inject electrons into ester bonds, forming radical anions that undergo selective C–O bond cleavage under mild conditions [154–156]. This mechanism bypasses the need for strong acids, bases, or high temperatures and demonstrates that PET depolymerization can proceed through electronically activated pathways rather than purely thermochemical routes. In parallel, robust non-metallic anodes such as boron-doped diamond represent another emerging direction, where extremely wide electrochemical windows and inert surfaces enable aggressive oxidative degradation of PET through hydroxyl radical generation and direct electron abstraction, driving polymer backbone scission toward deep oxidation and mineralization [157–159]. While such approaches emphasize degradation efficiency over selectivity, they highlight the role of electrode electronic structure and stability in governing the extent of oxidation. More recently, advanced coordination materials including metal–organic frameworks and single-atom catalysts have introduced a level of structural precision that bridges molecular catalysis and heterogeneous electrocatalysis. Three-dimensional MOF architectures provide well-defined metal coordination environments and accessible channels that enhance mass transport and stabilize high-valence intermediates for PET-derived ethylene glycol oxidation, while dual single-atom catalysts demonstrate how atomic-level synergy can decouple C–C bond cleavage from C–O oxidation, enabling highly selective conversion to value-added products such as glycolic acid [160–162]. Collectively, these emerging materials underscore a unifying principle: by precisely engineering electron-transfer pathways, active-site geometry, and intermediate stabilization beyond traditional lattice oxides, it becomes possible to transcend the intrinsic limitations of crystallinity-dominated PET degradation and unlock new regimes of selectivity, efficiency, and functional upcycling.

In addition to traditional catalytic methods, electro-organocatalytic strategies have emerged as a promising alternative, enabling PET depolymerization under mild conditions by utilizing single-electron transfer to activate ester bonds. Pham et al. reported an electricity-driven electro-organocatalytic strategy for direct PET depolymerization via single-electron transfer under mild conditions [142]. The schematic illustrates a redox-mediated electro-organocatalytic cycle, in which electrochemically generated organic electron donors initiate one-electron reduction of ester bonds in PET, enabling radical-induced C–O bond cleavage without harsh reagents (Figure 9a). Cyclic voltammetry shows distinct reduction features for PET in MeCN electrolyte compared with the solvent blank, confirming that PET can be directly activated through mediated electron transfer rather than nonspecific electroreduction (Figure 9b). Further comparison reveals enhanced cathodic currents in PET-containing systems relative to MeCN alone, demonstrating efficient formation of ester radical anions that underpin the electro-organocatalytic depolymerization pathway (Figure 9c). Beyond electro-organocatalytic depolymerization, direct electrochemical oxidation using robust anode materials, such as boron-doped diamond, provides an alternative pathway to degrade PET through strong oxidative processes. Gangadharan et al. investigated an electrochemical oxidation strategy using a boron-doped diamond (BDD) anode to directly degrade PET microplastics under near-neutral conditions [141]. The surface morphology of PET microplastics after electro-oxidation shows pronounced cracking, cavitation, and fragmentation compared with the smooth pristine particles, indicating severe polymer backbone disruption induced by oxidative attack (Figure 9d). The removal efficiency of PET microplastics increases steadily with reaction time and initial concentration, demonstrating that prolonged electro-oxidation enables progressive chain scission and mass loss rather than surface-limited erosion (Figure 9e). Total current efficiency and total organic carbon analyses reveal a continuous decrease during electro-oxidation, confirming that PET degradation proceeds toward deep oxidation and mineralization rather than partial surface modification (Figure 9f).

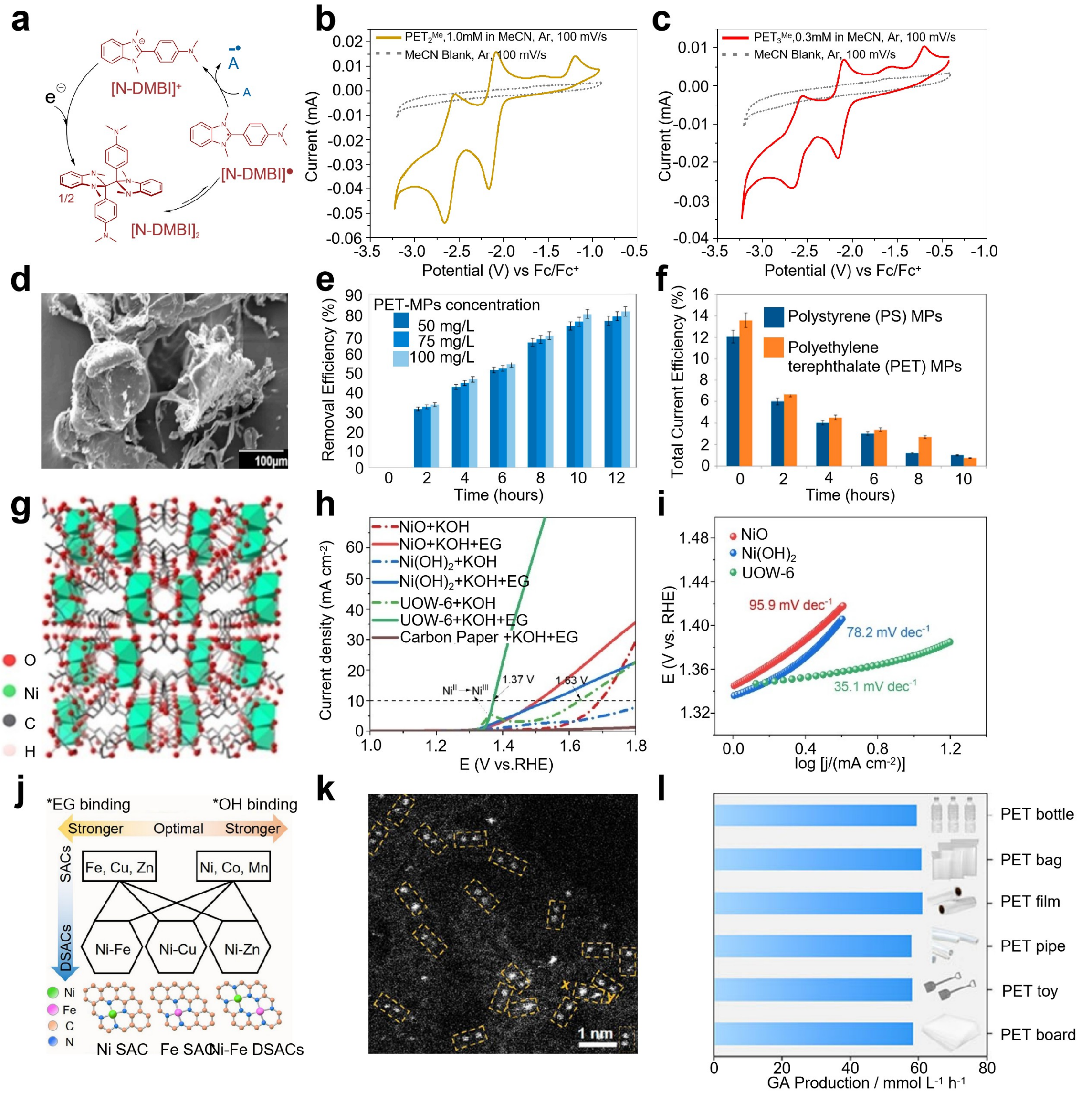

Figure 9. (**a**) Schematic of the electrochemical reduction process of PET model compound (PET2Me) mediated by [N-DMBI]$_2$, one-electron reduction steps leading to PET depolymerization. (**b**) Cyclic voltammogram of PET2Me

(1.0 mM in MeCN), redox peaks at approximately −2.1 V vs. Fc/Fc^+, reduction of ester bonds, baseline in MeCN under an inert atmosphere. (**c**) Cyclic voltammogram of PET2Me (0.3 mM in MeCN), redox behavior at more negative potentials, similar reduction feature compared to the higher concentration measurement. Reproduced with permission from Ref. [142]. Copyright 2023, Elsevier. (**d**) Scanning electron microscopy (SEM) image of PET microplastics, irregular shape and structure of the particles, Scale bar: 100 µm. (**e**) Removal efficiency of PET microplastics (PET-MPs) at concentrations of 50, 75, and 100 mg L^{-1} over 12 h, increased efficiency with higher concentrations. (**f**) Comparison of the total current efficiency for polystyrene (PS) and polyethylene terephthalate (PET) microplastics over time, higher current efficiency for PS compared to PET under the same experimental conditions. Reproduced with permission from Ref. [141]. Copyright 2025, Elsevier. (**g**) Schematic of the local structure of NiO and $Ni(OH)_2$ within the MOF, coordination environment and metal-ligand interactions. (**h**) Linear sweep voltammetry (LSV) curves of NiO, $Ni(OH)_2$, UOW-6, and carbon paper as catalysts in 1 M KOH and EG solutions, lower onset potential and enhanced catalytic activity of UOW-6 for ethylene glycol oxidation. (**i**) Tafel plots of NiO, $Ni(OH)_2$, and UOW-6 during ethylene glycol oxidation, kinetic behavior, smallest Tafel slope of UOW-6, faster electron transfer kinetics. Reproduced with permission from Ref. [139]. Copyright 2024, John Wiley and Sons. (**j**) Illustration of Ni-Fe dual-site active centers for EG and ·OH binding, optimized catalytic performance. (**k**) High-resolution TEM image of Ni-Fe DSACs, atomic arrangement with Fe atoms positioned adjacent to Ni atoms, enhanced EG oxidation efficiency. (**l**) GA production efficiency from different PET plastic forms (bottle, bag, film, pipe, toy, board), variation in catalytic efficiency for PET upcycling. Reproduced with permission from Ref. [134]. Copyright 2025, John Wiley and Sons.

Building on the success of electrochemical oxidation, the integration of metal–organic frameworks (MOFs) such as Ni-based UOW-6 further enhances the catalytic efficiency for PET-derived ethylene glycol oxidation, showcasing the potential of advanced materials for improving reaction kinetics and selectivity. Das et al. reported a biomass-derived Ni-based metal–organic framework (UOW-6) as an anodic catalyst for PET-derived ethylene glycol oxidation coupled with hydrogen evolution [139]. The crystal structure reveals a three-dimensionally connected Ni-MOF framework with well-defined Ni coordination environments, providing abundant accessible metal sites and structural stability under alkaline electrolysis conditions (Figure 9g). Electrochemical polarization curves show that UOW-6 delivers a significantly reduced EGOR onset potential and higher current density compared with NiO and $Ni(OH)_2$, indicating more favorable reaction kinetics enabled by the MOF architecture (Figure 9h). Tafel analysis further demonstrates a markedly smaller slope for UOW-6, confirming accelerated charge transfer and improved intrinsic catalytic activity for EG oxidation (Figure 9i). Expanding on the advancements in MOF-based catalysts, the design of dual single-atom catalysts, like Ni_1–Fe_1–N–C, offers exceptional selectivity and efficiency for glycolic acid formation, demonstrating the power of atomic-level synergy in optimizing PET oxidation. Yue et al. reported a Ni–Fe dual single-atom catalyst (Ni_1–Fe_1–N–C) to enable highly selective EG oxidation toward glycolic acid via dual-site synergy [134]. Density functional theory–guided analysis reveals that spatially adjacent Ni and Fe single atoms provide complementary adsorption sites, where Fe preferentially stabilizes *EG-derived intermediates while Ni favors *OH activation, establishing an optimal balance for selective C_2 oxidation (Figure 9j). Atomic-resolution STEM and spectroscopic characterization confirm the atomically dispersed Ni–Fe dual sites anchored on N-doped carbon, excluding nanoparticle or alloy formation and validating the designed dual-site configuration (Figure 9k). Electrochemical evaluation demonstrates that Ni_1–Fe_1–N–C achieves high GA selectivity (>90%) with a Faradaic efficiency up to ~96% at low overpotential, outperforming single-atom counterparts and highlighting the decisive role of Ni–Fe cooperative catalysis in suppressing C–C cleavage (Figure 9l).

5. Summary, Challenges, and Perspectives

In summary, this review provides a comprehensive, fiber-oriented perspective on PET degradation that contrasts with prior studies centered on bulk plastics. The discussion highlights the unique interfacial challenges introduced by fiber manufacturing and finishing, and emphasizes the decisive role of pretreatment in enabling efficient electrocatalysis, an aspect often overlooked previously. Electrocatalytic degradation is examined through a structural lens, with catalysts categorized by material family, crystallinity, composition, and interfacial characteristics. This approach offers a structure–performance view that supports cross-comparison and rational design. The consolidation of reported systems into standardized datasets further underscores the value of unifying diverse studies under common descriptors and evaluation metrics. Taken together, these elements establish the distinctiveness of this review in addressing PET fibers rather than bulk PET, in stressing interface and pretreatment effects, and in proposing a structure-centric taxonomy of catalysts.

Despite these advances, several critical challenges remain before electrocatalytic PET fiber degradation can transition from laboratory studies to practical implementation. At the materials level, most reported catalysts still face trade-offs between activity, selectivity, and durability; while defects, vacancies, or heterojunctions improve reactivity, they also accelerate structural reconstruction and leaching, particularly in the presence of dyes, finishing agents, or heavy metals common in real textile waste. On the process side, pretreatment has not been standardized, and the diversity of industrial finishing protocols results in fibers with highly variable wettability, crystallinity, and surface chemistry, making it difficult to compare results across studies or to optimize conditions systematically. At the mechanistic level, the interplay between radical flux, interfacial adsorption, and mass transport through hierarchical fiber bundles is still poorly quantified, and without clear kinetic models it remains challenging to predict selectivity windows that favor ester bond cleavage without over-oxidizing aromatic rings. Moreover, the majority of studies evaluate catalysts in batch cells with simple electrolytes, whereas scalable applications will require continuous-flow systems that manage large surface areas, fiber entanglement, and complex wastewater matrices [163,164], particularly as future textile systems trend toward increasingly sophisticated multilayer and optically functional designs [165]. Finally, techno-economic and environmental assessments are scarce; the true sustainability of these processes hinges on minimizing energy consumption, ensuring monomer purity, and integrating with existing textile recycling infrastructure [166]. Consequently, establishing a rigorous cost-benefit framework is imperative. future research should prioritize multi-scenario sensitivity analysis to quantify the trade-offs between electrochemical overpotentials and the market value of recovered terephthalic acid, while accounting for potential carbon credit incentives that define the economic tipping point for industrial upscaling. Addressing these interlinked challenges will be essential for translating promising electrocatalytic pathways into robust technologies capable of handling the heterogeneity and volume of global PET fiber waste.

Looking forward, future progress in electrocatalytic PET fiber degradation will depend on integrating insights from polymer science, surface chemistry, and electrochemical engineering into a unified design framework [167]. At the fiber level, systematic correlations between pretreatment strategies, crystallinity reduction, and interfacial wettability need to be established to rationalize how textile-specific variables govern degradation efficiency. At the catalyst level, emphasis should shift toward descriptor-driven design, where crystallinity, composition, and interfacial properties are quantitatively linked to radical generation, adsorption selectivity, and long-term stability, enabling predictive screening of materials rather than empirical selection. On the reactor side, the development of continuous-flow architectures with engineered three-phase boundaries, controllable mass transport, and energy-efficient current distribution will be indispensable for scaling laboratory findings to industrial textile waste streams. Beyond technical advances, coupling electrocatalysis with renewable electricity, circular monomer recovery, and life-cycle assessment will be critical to validate the environmental and economic viability of this approach. By addressing these aspects in parallel, the field can move from proof-of-concept studies toward robust, fiber-specific recycling technologies that not only mitigate plastic pollution but also provide a sustainable feedstock base for the textile industry of the future.

Author Contributions

R.C.: conceptualization, formal analysis, data curation, writing—original draft; J.L.: formal analysis, data curation, writing—original draft; K.Z.: conceptualization, formal analysis, data curation, software; A.Z.: software; W.X.: funding acquisition; H.W.: conceptualization, supervision, validation, writing—review & editing; J.W.: conceptualization, funding acquisition, supervision, validation, writing—review & editing. All authors have read and agreed to the published version of the manuscript.

Funding

This research was funded by the National Natural Science Foundation of China (52203070), and the Natural Science Foundation of Hubei Province (2025AFB863).

Institutional Review Board Statement

Not applicable.

Informed Consent Statement

Not applicable.

Data Availability Statement

The data are available from the corresponding author on reasonable request.

Conflicts of Interest

The authors declare no conflict of interest.

Use of AI and AI-Assisted Technologies

During the preparation of this work, the authors used Grammarly solely for English language editing to improve grammar, spelling, punctuation, and readability. After using this service, the authors carefully reviewed and edited the manuscript as needed and take full responsibility for the content of the published article. No AI tools were used for the generation, analysis, interpretation, or presentation of scientific data, the preparation of figures, or any other scientific content. All figures and graphical illustrations were independently created by the authors using professional software, including Autodesk 3ds Max, KeyShot, and other conventional graphics and visualization tools.

References

1. Fang, G.; Ma, X.; Hu, R.; et al. Horizontally Oriented 2D Skin Structures on Fiber Interface for Long-Life Flexible Energy Storage Devices. *Chem. Eng. J.* **2025**, *509*, 161557. https://doi.org/10.1016/j.cej.2025.161557.
2. Yang, R.; Xu, G.; Tao, W.; et al. Recycled Polymer: Green Roads for Polyester Plastics. *Green Carbon* **2024**, *2*, 1–11. https://doi.org/10.1016/j.greenca.2024.01.004.
3. Ma, X.; Wu, Z.; Tian, H.; et al. Durable Coaxial Fiber-Based Underwater Strain Sensor with Reversible Dry-Wet Transition. *Infomat* **2025**, *7*, e70030. https://doi.org/10.1002/inf2.70030.
4. Liu, Y.-J.; Zhou, J.; Li, Y.; et al. State-of-the-Art Advances in Biotechnology for Polyethylene Terephthalate Bio-Depolymerization. *Green Carbon* **2025**, *3*, 303–319. https://doi.org/10.1016/j.greenca.2025.02.003.
5. Huang, J.; Tian, H.; Zhang, H.; et al. Engineering Materials and Structural Paradigms for Mid-Infrared Thermal Management. *Mater. Today Energy* **2025**, *52*, 101944. https://doi.org/10.1016/j.mtener.2025.101944.
6. Yang, X.; Li, C.; Song, H.; et al. CeO_2/CoNiP Heterojunction as Excellent OER Electrocatalysts in Alkaline Seawater Effectively Suppresses Chloride Corrosion and Cobalt Leaching. *ACS Sustain. Chem. Eng.* **2025**, *13*, 13561–13572. https://doi.org/10.1021/acssuschemeng.5c05804.
7. Cai, J.; Wu, Z.; Wang, S.; et al. Exploring Advanced Microwave Strategy for the Synthesis of Two-Dimensional Energy Materials. *Appl. Phys. Rev.* **2024**, *11*, 021407. https://doi.org/10.1063/5.0231081.
8. Jiang, H.; Li, J.; Xiao, Z.; et al. The Rapid Production of Multiple Transition Metal Carbides via Microwave Combustion under Ambient Conditions. *Nanoscale* **2020**, *12*, 16245–16252. https://doi.org/10.1039/D0NR05223J.
9. Gandionco, K.A.; Kim, J.; Bekaert, L.; et al. Single-Atom Catalysts for the Electrochemical Reduction of Carbon Dioxide into Hydrocarbons and Oxygenates. *Carbon Energy* **2024**, *6*, e410. https://doi.org/10.1002/cey2.410.
10. Kim, M.; Joung, S.; Lee, S.; et al. Recent Advances in Ni-Based Electrocatalysts for Low-Energy Hydrogen Production via Alternative Pathways to Water Electrolysis. *Energy Mater.* **2025**, *5*, 500015. https://doi.org/10.20517/energymater.2024.244.
11. Feng, Y.; Wang, M.; Zhang, H.; et al. Engineering Electrocatalytic Structures Through Molten Salt-Mediated Mechanistic Control. *EcoEnergy* **2025**, *3*, e70022. https://doi.org/10.1002/ece2.70022.
12. Li, Q.; Fang, G.; Wu, Z.; et al. Advanced Microwave Strategies Facilitate Structural Engineering for Efficient Electrocatalysis. *ChemSusChem* **2024**, *17*, e202301874. https://doi.org/10.1002/cssc.202301874.
13. Zhang, D.; Pan, W.; Sharma, A.; et al. Over 14% Unassisted Water Splitting Driven by Immersed Perovskite/Si Tandem Photoanode with Ni-Based Catalysts. *Mater. Today Energy* **2025**, *48*, 101809. https://doi.org/10.1016/j.mtener.2025.101809.
14. Wang, K.; Wang, G.; Liu, Y.; et al. Regulation of Electrocatalytic Properties of High Entropy Alloy Electrocatalysts for the Oxygen Evolution Reaction. *J. Mater. Chem. A* **2024**, *12*, 29311–29334. https://doi.org/10.1039/D4TA04984E.
15. Li, Y.; Li, T.; Zhang, T.; et al. Artificial Skin Sensation for Neuroprosthetic Hands. *FlexMat* **2025**, *2*, 458–474. https://doi.org/10.1002/flm2.70019.
16. Ma, Y.; Qin, C.; Lei, Y.; et al. Tissue-Seeking Dyes for *in Vivo* Applications. *Smart Mol.* **2024**, *2*, e20240029. https://doi.org/10.1002/smo.20240029.
17. Zhang, S.; Gong, J.; Rong, Z.; et al. Blade Coating Large-Area 3D/1D Perovskite Heterojunction Films for Effective Synaptic Memristors. *Int. J. Min. Met. Mater.* **2025**, *32*, 498–503. https://doi.org/10.1007/s12613-025-3327-z.
18. Wang, K.; Liang, J.; Li, Z.; et al. Design of Experiments with the Support of Machine Learning for Process Parameter Optimization of All-Small-Molecule Organic Solar Cells. *FlexMat* **2024**, *1*, 234–247. https://doi.org/10.1002/flm2.34.

19. Lin, Y.; Huang, Y.; Wang, T.; et al. Bioinspired Flexible Photonic Sensing Chips for Wearable Multiparameter Monitoring. *FlexMat* **2025**, *2*, 365–389. https://doi.org/10.1002/flm2.70007.
20. Zhang, R.; Kong, X.; Ren, R.; et al. Recent Advances in Copper-Based Catalysts for Electrochemical Carbon Dioxide Reduction to C_2^+ Products. *Carbon Neutralization* **2025**, *4*, e70041. https://doi.org/10.1002/cnl2.70041.
21. Ren, Y.; Yu, F.; Li, X.-G.; et al. Soft–Hard Interface Design in Super-Elastic Conductive Polymer Hydrogel Containing Prussian Blue Analogues to Enable Highly Efficient Electrochemical Deionization. *Mater. Horiz.* **2023**, *10*, 3548–3558. https://doi.org/10.1039/D2MH01149B.
22. Wang, J.; Li, M.; Gao, H.; et al. Photoresponsive Tetracoordinate Arylboron Smart Molecules: Strategies for Molecular Design and Photoresponse Mechanisms. *Smart Mol.* **2024**, *2*, e20240041. https://doi.org/10.1002/smo.20240041.
23. Li, J.; Jiang, H.; Zhou, Q.; et al. Best Available Technology Options for the Mitigation of Environmental Impacts in Waste Plastics. *Carbon Neutrality* **2024**, *3*, 29. https://doi.org/10.1007/s43979-024-00102-x.
24. Liu, N.; Liu, D.; Zhan, Y.; et al. From Innovation to Integration: The Evolving Role of Carbon Capture and Storage in Global Decarbonization. *cScience* **2025**, *1*, e70008. https://doi.org/10.1002/csc3.70008.
25. Qinyun, X.; Keli, Y.; Laodong, G.; et al. Diatom Biorefinery: Comprehensive Resource Utilization and Economic Feasibility for Sustainable Development. *Sustain. Eng. Novit* **2025**, *1*, 3. https://doi.org/10.53941/sen.2025.100003.
26. Fan, M.; Tian, H.; Wu, Z.; et al. Microwave Shock Synthesis of Porous 2D Non-Layered Transition Metal Carbides for Efficient Hydrogen Evolution. *SusMat* **2025**, *5*, e252. https://doi.org/10.1002/sus2.252.
27. Du, M.; Chen, Y.; Mai, M.; et al. Understanding and Modulating the Horizontal Orientations and Short-Range Charge Transfer Excited States for High-Performance Narrowband Emitters. *FlexMat* **2024**, *1*, 46–53. https://doi.org/10.1002/flm2.15.
28. Huang, J.; Clark, A.H.; Hales, N.; et al. Spectroscopic Investigations of Complex Electronic Interactions by Elemental Doping and Material Compositing of Cobalt Oxide for Enhanced Oxygen Evolution Reaction Activity. *Adv. Funct. Mater.* **2024**, *34*, 2405384. https://doi.org/10.1002/adfm.202405384.
29. Li, H.; Chen, C.; Ye, Z.; et al. Purely Organic Room Temperature Phosphorescent Materials toward Organic Light-Emitting Diodes. *FlexMat* **2024**, *1*, 173–192. https://doi.org/10.1002/flm2.23.
30. Liu, Q.; Zhu, Z.; Zhang, H.; et al. Advanced Warming Textiles for Personalized Thermal Management through Radiative, Insulating, and Electrothermal Strategies. *Mater. Today Energy* **2026**, *56*, 102192. https://doi.org/10.1016/j.mtener.2026.102192.
31. Xu, R.; Zhu, Z.; Zhang, H.; et al. Synergistic Material-Structure Engineering for Mid-Infrared Thermal Management in Textiles. *Small* **2025**, *21*, 2509257. https://doi.org/10.1002/smll.202509257.
32. Wang, X.; Liu, T.; Sun, F.; et al. Highly Tough, Crack-Resistant and Self-Healable Piezo-Ionic Skin Enabled by Dynamic Hard Domains with Mechanosensitive Ionic Channel. *Smart Mol.* **2024**, *2*, e20240008. https://doi.org/10.1002/smo.20240008.
33. Ruiying, F.; Lianchao, W.; Xutian, Y.; et al. Defects-Engineered Metal-Organic Frameworks for Supercapacitor Platform. *Sustain. Eng. Novit* **2025**, *1*, 2. https://doi.org/10.53941/sen.2025.100002.
34. Chen, J.; Chu, L. AB Epoxy Encapsulation-Induced Transparency in Perovskite Films. *Sci. China Mater.* **2026**, *69*, 570–574. https://doi.org/10.1007/s40843-025-3552-2.
35. Takai, L.; Kinoshita, Y.; Takahashi, N.; et al. n-Type Carbon Nanotube Inks for High-Yield Printing of Ultrabroadband Soft Photo-Imager Thin Sheets. *FlexMat* **2025**, *2*, 115–125. https://doi.org/10.1002/flm2.41.
36. Kuanhong, C.; Guangshu, Y.; Mingxuan, L.; et al. Organoselenium Catalyzed Reaction: Sustainable Chemistry from Laboratory to Industry. *Sustain. Eng. Novit* **2025**, *1*, 1. https://doi.org/10.53941/sen.2025.100001.
37. Yang, J.; Cui, M.; Deng, J.; et al. Mild and Efficient Stripping of Blended Cotton-Polyester Fabrics Based on an Extended Acetolysis System. *Carbon Neutrality* **2025**, *4*, 40. https://doi.org/10.1007/s43979-025-00154-7.
38. Chauhan, M.; Budania, Y.; Modi, A.; et al. Trifunctional Nature of Heteroatom (B, N, S, O)-Doped Waste Diesel Soot: Turning Pollutants into Potential Energy Catalysts for HER, OER, and ORR. *Carbon Neutralization* **2025**, *4*, e195. https://doi.org/10.1002/cnl2.195.
39. Liu, L.; Gan, M.; Fan, X.; et al. Ultrasound-Assisted Capture of CO_2 from Flue Gas Using Steel Slag Leachate and Synthesis of Vaterite-Type $CaCO_3$. *cScience* **2025**, *1*, e70006. https://doi.org/10.1002/csc3.70006.
40. Tu, X.; Liu, X.; Zhang, Y.; et al. Advances in Sn-Based Oxide Catalysts for the Electroreduction of CO_2 to Formate. *Green Carbon* **2024**, *2*, 131–148. https://doi.org/10.1016/j.greenca.2024.03.006.
41. Quílez-Bermejo, J.; Herranz, J. A Review on Electrochemical CO_2-to-CH_4 Conversion for a Sustainable Energy Future: From Electrocatalysts to Electrolyzers. *J. Mater. Chem. A* **2025**, *13*, 41555–41579. https://doi.org/10.1039/D5TA03854E.
42. Gao, Z.; Xie, H.; Yang, X.; et al. Electric Vehicle Lifecycle Carbon Emission Reduction: A Review. *Carbon Neutralization* **2023**, *2*, 528–550. https://doi.org/10.1002/cnl2.81.
43. Mao, H.; Zhang, S.; Liu, J.; et al. Bimetallic Ions Modified 2-Methylimidazolium Functionalized Polypyrrole/Graphene Oxide for the Improved Supercapacitor. *FlexMat* **2024**, *1*, 302–310. https://doi.org/10.1002/flm2.32.

44. Li, J.; Orbell, W.; Li, X.; et al. Resolving the Activity–Selectivity Trade-Off in NH_3 Oxidation with an Intermetallic-Oxide Dual-Site Catalyst. *Adv. Funct. Mater.* **2026**, *36*, e30020. https://doi.org/10.1002/adfm.202530020.
45. Meskher, H.; Woldu, A.R.; Chu, P.K.; et al. Sustainability Assessment of Seawater Splitting: Prospects, Challenges, and Future Directions. *EcoEnergy* **2024**, *2*, 630–651. https://doi.org/10.1002/ece2.68.
46. Fan, C.; Pan, F.; Ma, S.; et al. Hydrogen Direct Reduction: History and Pathways for Cost Reduction. *cScience* **2025**, *1*, e70003. https://doi.org/10.1002/csc3.70003.
47. Li, W.; Xu, Y.; Wang, G.; et al. Sustainable Carbon-Based Catalyst Materials Derived from Lignocellulosic Biomass for Energy Storage and Conversion: Atomic Modulation and Properties Improvement. *Carbon Energy* **2025**, *7*, e708. https://doi.org/10.1002/cey2.708.
48. Wan, J.; Fang, G.; Mi, S.; et al. Metastable 2D Amorphous Nb_2O_5 for Aqueous Supercapacitor Energy Storage. *Chem. Eng. J.* **2024**, *488*, 150912. https://doi.org/10.1016/j.cej.2024.150912.
49. Baig, M.M.; Khan, S.A.; Ahmad, H.; et al. 3D Printing of Hydrogels for Flexible Micro-Supercapacitors. *FlexMat* **2024**, *1*, 79–99. https://doi.org/10.1002/flm2.14.
50. Qin, S.; Dai, J.; Tian, H.; et al. 3D Printing Driving Innovations in Extreme Low-Temperature Energy Storage. *Virtual Phys. Prototyp.* **2025**, *20*, e2459798. https://doi.org/10.1080/17452759.2025.2459798.
51. Hu, R.; Wei, L.; Xian, J.; et al. Microwave Shock Process for Rapid Synthesis of 2D Porous $La_{0.2}Sr_{0.8}CoO_3$ Perovskite as an Efficient Oxygen Evolution Reaction Catalyst. *Acta Phys. Chim. Sin.* **2023**, *39*, 2212025. https://doi.org/10.3866/pku.Whxb202212025.
52. Feng, Y.; Dai, J.; Wang, M.; et al. Unraveling Metastable Perovskite Oxides: Insights from Structural Engineering to Synthesis Paradigms. *Microstructures* **2025**, *5*, 2025068. https://doi.org/10.20517/microstructures.2024.115.
53. Li, Z.; Wang, S.; Yin, Y.; et al. Electrooxidation of Ethylene Glycol to Glycolic Acid with Pt-Ni$(OH)_2$ Catalysts: High Efficiency and Selectivity for PET Plastics Upgrading. *Chem. Asian J.* **2025**, *20*, e202401843. https://doi.org/10.1002/asia.202401843.
54. Li, Y.; Yi, H.; Li, M.; et al. Synchronous Degradation and Decolorization of Colored Poly(ethylene terephthalate) Fabrics for the Synthesis of High Purity Terephthalic Acid. *J. Cleaner Prod.* **2022**, *366*, 132985. https://doi.org/10.1016/j.jclepro.2022.132985.
55. Wang, D.; Xu, H.; Tan, F.; et al. Boosting Simultaneous Proton Transfer and Oxygen-Related Radical Species Generation for H_2O_2 Photosynthesis by Cationic Polarization of Covalent Organic Polymers. *Chem. Eng. J.* **2025**, *524*, 169225. https://doi.org/10.1016/j.cej.2025.169225.
56. Su, Y.; Zhang, Y.; Feng, W.; et al. Monocarboxylic Acid Structural Analogues Facilitate *in Situ* Composite of Functional Complexes for Aqueous Batteries. *Angew. Chem. Int. Ed.* **2025**, *64*, e202502752. https://doi.org/10.1002/anie.202502752.
57. Chang, C.-W.; Ting, Y.-C.; Yen, F.-Y.; et al. High Performance Anion Exchange Membrane Water Electrolysis Driven by Atomic Scale Synergy of Non-Precious High Entropy Catalysts. *Energy Mater.* **2025**, *5*, 500042. https://doi.org/10.20517/energymater.2025.05.
58. Wu, X.; Chen, M.; Li, S.; et al. Sea Urchin-Like La-Doped MnO_2 for Electrocatalytic Oxidation Degradation of Sulfonamide in Water. *Energy Mater.* **2025**, *5*, 500089. https://doi.org/10.20517/energymater.2025.103.
59. Yang, X.; Zhang, Y.; Sun, P.; et al. A Review on Renewable Energy: Conversion and Utilization of Biomass. *Smart Mol.* **2024**, *2*, e20240019. https://doi.org/10.1002/smo.20240019.
60. Liu, Y.; Ma, J.; Yang, Y.; et al. Smart Chiral Liquid Crystal Elastomers: Design, Properties and Application. *Smart Mol.* **2024**, *2*, e20230025. https://doi.org/10.1002/smo.20230025.
61. Hu, K.; Li, B.; Tian, Z.; et al. Multiscale Simulation in Fuel Cell and Electrolyzer Systems: A Review of Methods, Applications, and Future Prospects. *Sustain. Eng. Novit* **2025**, *1*, 5. https://doi.org/10.53941/sen.2025.100005.
62. Liu, Y.; Liu, K.; Wang, P.; et al. Electrocatalytic Upcycling of Nitrogenous Wastes into Green Ammonia: Advances and Perspectives on Materials Innovation. *Carbon Neutrality* **2023**, *2*, 14. https://doi.org/10.1007/s43979-023-00055-7.
63. Han, Y.; Wang, J.; Liu, Y.; et al. Stability Challenges and Opportunities of NiFe-Based Electrocatalysts for Oxygen Evolution Reaction in Alkaline Media. *Carbon Neutralization* **2024**, *3*, 172–198. https://doi.org/10.1002/cnl2.110.
64. Huijie, Z.; Wenjiang, Z.; Shunyu, G.; et al. Multimodal Intelligence in Chemical Discovery: Integrating Interpretable ML, Autonomous Robotics, and Edge Computing. *Sustain. Eng. Novit* **2025**, *1*, 4. https://doi.org/10.53941/sen.2025.100004.
65. Rabiee, H.; Yan, P.; Wang, H.; et al. Electrochemical CO_2 Reduction Integrated with Membrane/Adsorption-Based CO_2 Capture in Gas-Diffusion Electrodes and Electrolytes. *EcoEnergy* **2024**, *2*, 3–21. https://doi.org/10.1002/ece2.23.
66. Yu, L.; Yiwen, Y.; Rui, W.; et al. Computational Studies for Aqueous Zinc-Ion Secondary Batteries. *Sustain. Eng. Novit* **2025**, *1*, 6. https://doi.org/10.53941/sen.2025.100006.
67. Zhao, Z.; Yao, X.; Zhang, L.; et al. Electrocatalytic Dehalogenation in the Applications of Organic Synthesis and Environmental Degradation. *EcoEnergy* **2024**, *2*, 83–113. https://doi.org/10.1002/ece2.28.

68. Chen, B.; Feng, M.; Chen, Y.; et al. Performing Electrocatalytic CO_2 Reduction Reactions at a High Pressure. *Carbon Neutrality* **2024**, *3*, 31. https://doi.org/10.1007/s43979-024-00106-7.
69. Liu, K.; Nawaz, M.A.; Liao, G. Progress and Future Challenges in Designing High-Performance Ni/CeO_2 Catalysts for CO_2 Methanation: A Critical Review. *Carbon Neutralization* **2025**, *4*, e190. https://doi.org/10.1002/cnl2.190.
70. Birat, J.-P.; Fick, G. Recent Advances in Life Cycle Assessment and Other Sustainability Metrics. *cScience* **2025**, *1*, e70007. https://doi.org/10.1002/csc3.70007.
71. McTernan, C.T.; Davies, J.A.; Nitschke, J.R. Beyond Platonic: How to Build Metal–Organic Polyhedra Capable of Binding Low-Symmetry, Information-Rich Molecular Cargoes. *Chem. Rev.* **2022**, *122*, 10393–10437. https://doi.org/10.1021/acs.chemrev.1c00763.
72. Zhai, Z.; Li, D.; Lu, X.; et al. Heteroatom-Induced Tensile Strain in Copper Lattice Boosts CO_2 Electroreduction toward Multi-Carbon Products. *Carbon Energy* **2024**, *6*, e648. https://doi.org/10.1002/cey2.648.
73. Zhang, C.; Gu, Y.; Jiang, Q.; et al. Exploration of Gas-Dependent Self-Adaptive Reconstruction Behavior of Cu_2O for Electrochemical CO_2 Conversion to Multi-Carbon Products. *Nano Micro Lett.* **2024**, *17*, 66. https://doi.org/10.1007/s40820-024-01568-1.
74. Lv, Z.; Jia, D.; Wei, J.; et al. Oxygen Atom-Driven COOH Formation Pathway on FeP/Cu_2O Heterostructure for Highly Selective Photoelectrochemical Reduction of CO_2 to CO. *Electrochim. Acta* **2026**, *552*, 148242. https://doi.org/10.1016/j.electacta.2026.148242.
75. Zhang, T.; Fan, H.J. Grafted Superstructure Renders Catalyst Stability in Alkaline Water Oxidation. *cScience* **2025**, *1*, e70000. https://doi.org/10.1002/csc3.70000.
76. Tian, Y.; Chen, R.; Liu, X.; et al. Highly Stabilized and Selective Ammonia Electro-Oxidation over CuNi Metallic Glass Nanoarray. *Carbon Energy* **2025**, *7*, e667. https://doi.org/10.1002/cey2.667.
77. Gu, Z.; Zhu, J.; Xue, Z.; et al. Challenges and Strategies for CO_2 Electroreduction to C_2^+ Products under Acidic Conditions. *Green Carbon* **2025**, *in press*. https://doi.org/10.1016/j.greenca.2025.07.002.
78. Dai, J.; Xian, J.; Liu, K.; et al. Unconventional Metastable Cubic 2D $LaMnO_3$ for Efficient Alkaline Seawater Oxygen Evolution. *Chin. J. Catal.* **2025**, *74*, 228–239. https://doi.org/10.1016/S1872-2067(25)64667-5.
79. Chen, C.; Jin, H.; Wang, P.; et al. Local Reaction Environment in Electrocatalysis. *Chem. Soc. Rev.* **2024**, *53*, 2022–2055. https://doi.org/10.1039/D3CS00669G.
80. Noh, K.J.; Park, B.J.; Wang, Y.; et al. Tailoring Local Structures of Atomically Dispersed Copper Sites for Highly Selective CO_2 Electroreduction. *Carbon Energy* **2024**, *6*, e419. https://doi.org/10.1002/cey2.419.
81. Fan, M.; Guo, J.; Fang, G.; et al. Microwave-Pulse Assisted Synthesis of Tunable Ternary-Doped 2D Molybdenum Carbide for Efficient Hydrogen Evolution. *Chem. Synth.* **2024**, *4*, 36. https://doi.org/10.20517/cs.2023.72.
82. Wu, Z.; Xian, J.; Dai, J.; et al. Microwave-Pulse Synthesis of Tunable 2D Porous Nickel-Enriched $LaMn_xNi_{1-x}O_3$ Solid Solution for Efficient Electrocatalytic Urea Oxidation. *J. Mater. Chem. A* **2024**, *12*, 7047–7057. https://doi.org/10.1039/d4ta00235k.
83. Zhang, H.; Qi, M.; Wang, Y. NiNC Catalysts in CO_2-to-CO Electrolysis. *Nano Micro Lett.* **2024**, *17*, 94. https://doi.org/10.1007/s40820-024-01595-y.
84. Hu, X.; Jiang, M.; Li, S. Synergy and Stability: The Rise of High-Entropy Single-Atom Catalysts. *Adv. Mater.* **2026**, *38*, e22135. https://doi.org/10.1002/adma.202522135.
85. Chen, Z.; Han, N.; Wei, W.; et al. Dual Doping: An Emerging Strategy to Construct Efficient Metal Catalysts for Water Electrolysis. *EcoEnergy* **2024**, *2*, 114–140. https://doi.org/10.1002/ece2.29.
86. Wang, S.; Zhang, M.; Mu, X.; et al. Atomically Dispersed Multi-Site Catalysts: Bifunctional Oxygen Electrocatalysts Boost Flexible Zinc–Air Battery Performance. *Energy Environ. Sci.* **2024**, *17*, 4847–4870. https://doi.org/10.1039/D4EE01656D.
87. Shan, L.; Liu, Y.; Chen, Y.; et al. High-Density Iron–Nickel Dual Sites in Carbon Aerogels as Effective Alkaline Water/Seawater Oxidation Electrocatalysts. *ACS Sustainable Chem. Eng.* **2025**, *13*, 311–320. https://doi.org/10.1021/acssuschemeng.4c07297.
88. Wu, B.; Harrath, K.; Sendeku, M.G.; et al. Electrochemical Evolution of a Metal Oxyhydroxide Surface on Two-Dimensional Layered Metal Phosphorus Trisulfides Enables the Oxidation of Amine to Nitrile. *Carbon Energy* **2025**, *7*, e672. https://doi.org/10.1002/cey2.672.
89. Dai, J.; Wang, M.; Tian, H.; et al. Microwave Shock-Driven Thermal Engineering of Unconventional Cubic 2D $LaMnO_3$ for Efficient Oxygen Evolution. *J. Mater. Chem. A* **2025**, *13*, 31002–31012. https://doi.org/10.1039/D5TA01034A.
90. Choe, S.; Kim, N.; Jang, Y.J. Perspective on the Interfacial Engineering for Electrocatalytic N_2 to NH_3 Conversion from Catalysts to Systems. *EcoEnergy* **2023**, *1*, 3–15. https://doi.org/10.1002/ece2.10.
91. Jiang, H.; Xian, J.; Hu, R.; et al. Microwave Discharge for Rapid Introduction of Bimetallic-Synergistic Configuration to Conductive Catecholate toward Long-Term Supercapacitor. *Chem. Eng. J.* **2023**, *455*, 140804. https://doi.org/10.1016/j.cej.2022.140804.

92. Zhao, Q.; Zhao, B.; Long, X.; et al. Interfacial Electronic Modulation of Dual-Monodispersed Pt–Ni_3S_2 as Efficacious Bi-Functional Electrocatalysts for Concurrent H_2 Evolution and Methanol Selective Oxidation. *Nano Micro Lett.* **2024**, *16*, 80. https://doi.org/10.1007/s40820-023-01282-4.
93. Faridi, S.; Razzaq, S.; Singh, D.; et al. Trends in Competing Oxygen and Chlorine Evolution Reactions over Electrochemically Formed Single-Atom Centers of MXenes. *J. Mater. Chem. A* **2025**, *13*, 16481–16490. https://doi.org/10.1039/D5TA02220G.
94. Mei, Z.; Zhou, Y.; Lv, W.; et al. Recent Progress in Electrocatalytic Urea Synthesis under Ambient Conditions. *ACS Sustain. Chem. Eng.* **2022**, *10*, 12477–12496. https://doi.org/10.1021/acssuschemeng.2c03681.
95. Kohan, E.; Khoshnavazi, R.; Hosseini, M.G.; et al. A Review on Instability Factors of Mono- and Divalent Metal Ion Batteries: From Fundamentals to Approaches. *J. Mater. Chem. A* **2024**, *12*, 30190–30248. https://doi.org/10.1039/D4TA05386A.
96. Chen, Y.; Jia, C.; Zhou, C.; et al. Electrocatalytic Polyester Waste Upcycling via Lattice Oxygen Redox Activation. *Angew. Chem. Int. Ed.* **2025**, *64*, e202513447. https://doi.org/10.1002/anie.202513447.
97. Qi, L.; Jiang, J.; Sun, Y.; et al. Ultra-Efficient Electrooxidation of Ethylene Glycol Enabled by Pd-Loaded Fe-Doped Nb_2O_5 with Abundant Oxygen Vacancies. *Chem. Eng. J.* **2023**, *475*, 146050. https://doi.org/10.1016/j.cej.2023.146050.
98. Li, Z.; Yang, Z.; Wang, S.; et al. Medium Entropy Metal Oxide Induced OH Species Targeted Transfer Strategy for Efficient Polyethylene Terephthalate Plastic Recycling. *Chem. Eng. J.* **2024**, *479*, 147611. https://doi.org/10.1016/j.cej.2023.147611.
99. Mari, E.; Tsai, P.; Eswaran, M.; et al. Efficient Electro-Catalytic Oxidation of Ethylene Glycol Using Flower-Like Graphitic Carbon Nitride/Iron Oxide/Palladium Nanocomposite for Fuel Cell Application. *Fuel* **2020**, *280*, 118646. https://doi.org/10.1016/j.fuel.2020.118646.
100. Wang, J.; Li, X.; Zhang, T.; et al. Electro-Reforming Polyethylene Terephthalate Plastic to Co-Produce Valued Chemicals and Green Hydrogen. *J. Phys. Chem. Lett.* **2022**, *13*, 622–627. https://doi.org/10.1021/acs.jpclett.1c03658.
101. Aladeemy, S.A.; AlRijraji, T.R.; Amer, M.S.; et al. Electrooxidation of Ethylene Glycol Coupled with Hydrogen Production on Porous NiO/Ni@NF Nanosheet Electrocatalysts. *Catal. Sci. Technol.* **2025**, *15*, 2571–2583. https://doi.org/10.1039/D4CY01450B.
102. Arjona, N.; Espinosa-Magaña, F.; Bañuelos, J.A.; et al. Manganese Oxides (Mn_3O_4 & α-MnO_2) as Co-Catalysts in Pd-Based Nanomaterials for the Ethylene Glycol Electro-Oxidation. *ChemElectroChem* **2022**, *9*, e202200015. https://doi.org/10.1002/celc.202200015.
103. Sultan, M.A.; Hassan, H.B.; Tammam, R.H. Stimulation of Ethylene Glycol Electrooxidation on Electrodeposited Ni–PbO_2–GN Nanocomposite in Alkaline Medium. *J. Appl. Electrochem.* **2023**, *53*, 463–486. https://doi.org/10.1007/s10800-022-01792-w.
104. Leiva-Leroy, C.; Koul, A.; Nkou, F.B.S.; et al. From Heat to Electrons: Bridging Heterogeneous Liquid-Phase Thermal and Electrocatalytic Oxidation of Ethylene Glycol over Co_3O_4. *Angew. Chem. Int. Ed.* **2026**, *65*, e19188. https://doi.org/10.1002/anie.202519188.
105. Wang, H.; Yang, B.; Smith, R.L., Jr.; et al. Electro-Reconstructed Transition Metal Electrodes for Coupled-Upgrading of Nitrate Pollution and Waste Poly(Ethylene Terephthalate) Plastics. *Adv. Funct. Mater.* **2025**, *35*, 2425333. https://doi.org/10.1002/adfm.202425333.
106. Mais, L.; Melis, N.; Vacca, A.; et al. Electrochemical Removal of PET and PE Microplastics for Wastewater Treatment. *Environ. Sci. Water Res. Technol.* **2024**, *10*, 399–407. https://doi.org/10.1039/D3EW00582H.
107. Sun, L.; Lv, H.; Xiao, J.; et al. Enzymatic Mesoporous Metal Nanocavities for Concurrent Electrocatalysis of Nitrate to Ammonia Coupled with Polyethylene Terephthalate Upcycling. *Adv. Mater.* **2024**, *36*, 2402767. https://doi.org/10.1002/adma.202402767.
108. Xin, L.; Zhang, Z.; Qi, J.; et al. Electrocatalytic Oxidation of Ethylene Glycol (EG) on Supported Pt and Au Catalysts in Alkaline Media: Reaction Pathway Investigation in Three-Electrode Cell and Fuel Cell Reactors. *Appl. Catal. B* **2012**, *125*, 85–94. https://doi.org/10.1016/j.apcatb.2012.05.024.
109. Ma, Y.; Guo, X.; Yuan, W.; et al. Paired Electrochemical Synthesis of Glycolic Acid and Ammonia from Polyester and Nitrate Sewage. *Chem Catal.* **2025**, *5*, 101336. https://doi.org/10.1016/j.checat.2025.101336.
110. Kang, S.; Yuan, W.; Guo, X.; et al. Concurrent Production of Glycolic Acid via Anode Valorization of Plastic Paired with Cathode Upcycling of Biomass Derivative. *Angew. Chem. Int. Ed.* **2025**, *64*, e202504993. https://doi.org/10.1002/anie.202504993.
111. Han, S.; Sun, L.; Fan, D.; et al. Pulsed Electrosynthesis of Glycolic Acid through Polyethylene Terephthalate Upcycling over a Mesoporous PdCu Catalyst. *Nat. Commun.* **2025**, *16*, 3426. https://doi.org/10.1038/s41467-025-58813-3.
112. Wang, S.; Li, S.; Li, Y.; et al. Electronic State Reconfiguration of $NiMoCo_x$ Boosts Electrocatalytic Upcycling of Polyethylene Terephthalate Plastic Wastes for Simultaneous Production of Formate and Green Hydrogen. *Chem. Eng. J.* **2025**, *515*, 163901. https://doi.org/10.1016/j.cej.2025.163901.
113. Si, D.; Xiong, B.; Chen, L.; et al. Highly Selective and Efficient Electrocatalytic Synthesis of Glycolic Acid in Coupling with Hydrogen Evolution. *Chem Catal.* **2021**, *1*, 941–955. https://doi.org/10.1016/j.checat.2021.08.001.

114. Chen, J.; Zhang, F.; Kuang, M.; et al. Unveiling Synergy of Strain and Ligand Effects in Metallic Aerogel for Electrocatalytic Polyethylene Terephthalate Upcycling. *Proc. Natl. Acad. Sci. USA* **2024**, *121*, e2318853121. https://doi.org/10.1073/pnas.2318853121.
115. Selvaraj, V.; Vinoba, M.; Alagar, M. Electrocatalytic Oxidation of Ethylene Glycol on Pt and Pt–Ru Nanoparticles Modified Multi-Walled Carbon Nanotubes. *J. Colloid Interface Sci.* **2008**, *322*, 537–544. https://doi.org/10.1016/j.jcis.2008.02.069.
116. Cheng, J.; Tu, Y.; Xiang, Y.; et al. Anti-Poisoning of CO and Carbonyl Species over Pd Catalysts during the Electrooxidation of Ethylene Glycol to Glycolic Acid at Elevated Current Density. *Chem. Sci.* **2025**, *16*, 4303–4310. https://doi.org/10.1039/D4SC08579E.
117. Ma, H.-Z.; He, S.-H.; Zhang, Y.; et al. Selective Electrocatalytic Oxidation of Ethylene Glycol into Glycolic Acid at Coin-Group Electrodes: An Investigation on Catalytic Activity and Selectivity. *ACS Sustain. Chem. Eng.* **2024**, *12*, 12249–12259. https://doi.org/10.1021/acssuschemeng.4c04928.
118. Guo, H.; Kang, J.; Du, Y.; et al. N-Coordinated Pd-Rh Synergy for Highly Selective Ethylene Glycol Oxidation and Efficient Hydrogen Evolution. *Green Chem.* **2025**, *27*, 7242–7253. https://doi.org/10.1039/d5gc00784d.
119. Li, W.; Bao, Q.; Ma, F.; et al. Metal-Support Interaction and Tip-Enhanced Electric Field Effect Co-Enhancing Oxygen Species Adsorption/Enrichment for Efficient Electrooxidation of Plastic Waste Derived Alcohol into Glycolic Acid. *Appl. Catal. B Environ.* **2025**, *374*, 125375. https://doi.org/10.1016/j.apcatb.2025.125375.
120. Wang, Z.; Li, J.; Zhang, Q.; et al. Facilitating Formate Selectivity via Optimizing e_g* Band Broadening in NiMn Hydroxides for Ethylene Glycol Electro-Oxidation. *Angew. Chem. Int. Ed.* **2024**, *63*, e202411517. https://doi.org/10.1002/anie.202411517.
121. Lu, X.; Guo, Y.; Fu, H.; et al. Electrochemical Upcycling Strategy for Polyethylene Terephthalate Plastic Coupled with Efficient Hydrogen Production. *Chem. Eng. J.* **2025**, *506*, 159810. https://doi.org/10.1016/j.cej.2025.159810.
122. Fang, Z.; Du, X.; Qian, K.; et al. Interfacial Effects in $Ni(OH)_2$/MnO@Ni Aerogel Heterostructures Promote Highly Efficient Electrooxidation of Ethylene Glycol to Formate and Hydrogen. *Int. J. Hydrogen Energy* **2024**, *74*, 39–48. https://doi.org/10.1016/j.ijhydene.2024.06.140.
123. Ma, Y.; Ge, H.; Zhang, Y.; et al. Selective Electrooxidation of Ethylene Glycol to Formate with Hydrogen Cogeneration in Ni_3S_2 Nanodomains on NiFeMn-LDH Nanosheet Arrays. *ACS Sustain. Chem. Eng.* **2025**, *13*, 5601–5612. https://doi.org/10.1021/acssuschemeng.4c10750.
124. Li, Y.; Liu, X.; Wang, K.; et al. Oxygen Vacancy Assisted Ru-$Ni(OH)_2$ for Efficient Ethylene Glycol Electrooxidation Reaction. *Inorg. Chem. Front.* **2024**, *11*, 6889–6897. https://doi.org/10.1039/d4qi01372g.
125. Fan, J.; Xu, B.; Cheng, C.; et al. Pd-Doped CoNi-Based Bifunctional Electrodes for Upcycling of PET Plastic with Ultra-Long Stability. *Appl. Catal. B Environ.* **2025**, *367*, 125076. https://doi.org/10.1016/j.apcatb.2025.125076.
126. Wang, N.; Li, X.; Hu, M.-K.; et al. Ordered Macroporous Superstructure of Bifunctional Cobalt Phosphide with Heteroatomic Modification for Paired Hydrogen Production and Polyethylene Terephthalate Plastic Recycling. *Appl. Catal. B* **2022**, *316*, 121667. https://doi.org/10.1016/j.apcatb.2022.121667.
127. Xia, T.; Chen, Z.; Dong, C.; et al. Yeast Inherited Phosphide/Bio-Carbon for Controllable Polyethylene Terephthalate Upcycling. *Adv. Funct. Mater.* **2025**, *35*, 2503193. https://doi.org/10.1002/adfm.202503193.
128. Zhou, H.; Ren, Y.; Li, Z.; et al. Electrocatalytic Upcycling of Polyethylene Terephthalate to Commodity Chemicals and H_2 Fuel. *Nat. Commun.* **2021**, *12*, 4679. https://doi.org/10.1038/s41467-021-25048-x.
129. Yu, Z.; Xu, J.; Amorim, I.; et al. Easy Preparation of Multifunctional Ternary PdNiP/C Catalysts toward Enhanced Small Organic Molecule Electro-Oxidation and Hydrogen Evolution Reactions. *J. Energy Chem.* **2021**, *58*, 256–263. https://doi.org/10.1016/j.jechem.2020.10.016.
130. Zhang, J.; Zhang, X.; Shi, C.; et al. Plasma-Constructed Co_2P-Ni_2P Heterointerface for Electro-Upcycling of Polyethylene Terephthalate Plastic to Co-Produce Hydrogen and Formate. *Small* **2024**, *20*, 2406767. https://doi.org/10.1002/smll.202406767.
131. Chang, J.; Wang, L.; Wu, D.; et al. Concurrent Electrocatalytic Hydrogen Evolution and Polyethylene Terephthalate Plastics Reforming by Self-Supported Amorphous Cobalt Iron Phosphide Electrode. *J. Colloid Interface Sci.* **2024**, *655*, 555–564. https://doi.org/10.1016/j.jcis.2023.11.044.
132. Ghosh, S.; Mondal, B.; Roy, S.; et al. Alcohol Oxidation with High Efficiency and Selectivity by Nickel Phosphide Phases. *J. Mater. Chem. A* **2022**, *10*, 8238–8244. https://doi.org/10.1039/D2TA00863G.
133. Ma, G.; Yang, N.; Xue, Y.; et al. Ethylene Glycol Electrochemical Reforming Using Ruthenium Nanoparticle-Decorated Nickel Phosphide Ultrathin Nanosheets. *ACS Appl. Mater. Interfaces* **2021**, *13*, 42763–42772. https://doi.org/10.1021/acsami.1c10971.
134. Yue, S.; Zhao, Z.; Liu, Y.; et al. Dual-Site Synergistic Electrocatalysis Enables Highly Selective Upcycling of Real-World Plastic Waste to Glycolic Acid. *Adv. Funct. Mater.* **2025**, *35*, 2509766. https://doi.org/10.1002/adfm.202509766.
135. Ma, Y.; Li, L.; Tang, J.; et al. Electrochemical PET Recycling to Formate through Ethylene Glycol Oxidation on Ni-Co-S Nanosheet Arrays. *J. Mater. Chem. A* **2024**, *12*, 33917–33925. https://doi.org/10.1039/d4ta07156e.

136. Li, J.; Li, L.; Ma, X.; et al. Selective Ethylene Glycol Oxidation to Formate on Nickel Selenide with Simultaneous Evolution of Hydrogen. *Adv. Sci.* **2023**, *10*, 2300841. https://doi.org/10.1002/advs.202300841.
137. Behera, S.; Dinda, S.; Saha, R.; et al. Quantitative Electrocatalytic Upcycling of Polyethylene Terephthalate Plastic and Its Oligomer with a Cobalt-Based One-Dimensional Coordination Polymer Having Open Metal Sites along with Coproduction of Hydrogen. *ACS Catal.* **2023**, *13*, 469–474. https://doi.org/10.1021/acscatal.2c05270.
138. Li, M.; Xia, T.; Wang, M.; et al. Biocarbon-Confined Bimetallic FeCo Metal-Organic Framework Orthogonal Nanosheet Arrays for Industry-Level Ethylene Glycol Oxidation. *Chin. J. Struct. Chem.* **2025**, *44*, 100627. https://doi.org/10.1016/j.cjsc.2025.100627.
139. Das, S.; Zhang, T.; Clarkson, G.; et al. Selective Electrocatalytic Production of Formic Acid from Plastic Waste Using a Nickel Metal-Organic Framework Constructed from a Biomass-Derived Ligand. *ChemSusChem* **2025**, *18*, e202402319. https://doi.org/10.1002/cssc.202402319.
140. Guo, Z.; Liu, M.; Ga, L.; et al. Terbium-Doped Cobalt-Based Metal-Organic Frameworks for Electrocatalytic Hydrogen Production and Polyethylene Terephthalate Plastic Upcycling. *Chem. Eng. J.* **2024**, *496*, 154062. https://doi.org/10.1016/j.cej.2024.154062.
141. Gangadharan, P.G.; Bharti, A.; Sengupta, S.; et al. Enhancing the Degradation of Polystyrene and Polyethylene Terephthalate Microplastics in Water Using Electrochemical Treatment at Neutral pH. *J. Environ. Manag.* **2025**, *394*, 127401. https://doi.org/10.1016/j.jenvman.2025.127401.
142. Pham, P.H.; Barlow, S.; Marder, S.R.; et al. Electricity-Driven Recycling of Ester Plastics Using One-Electron Electro-Organocatalysis. *Chem Catal.* **2023**, *3*, 100675. https://doi.org/10.1016/j.checat.2023.100675.
143. Chen, R.; Zhang, Z.; Deng, Y.; et al. Electrochemical Degradation of PET Microplastics and Its Mechanism. *Ind. Eng. Chem. Res.* **2025**, *64*, 7915–7929. https://doi.org/10.1021/acs.iecr.5c00311.
144. Mohanty, D.; Kuan, W.-F. Recent Advances in Carbon-Based Electrocatalysts for Rechargeable Li-CO_2 Batteries: A Review. *Mater. Today Energy* **2025**, *54*, 102095. https://doi.org/10.1016/j.mtener.2025.102095.
145. Wang, K.; Yun, S.; Sun, M.; et al. Strengthening Heterogeneous Strain in FeCoNiMo-Based High-Entropy Alloys for Advanced Energy Conversion. *Mater. Today Energy* **2025**, *48*, 101762. https://doi.org/10.1016/j.mtener.2024.101762.
146. Jin, J.; Wang, X.; Hu, Y.; et al. Precisely Control Relationship between Sulfur Vacancy and H Absorption for Boosting Hydrogen Evolution Reaction. *Nano Micro Lett.* **2024**, *16*, 63. https://doi.org/10.1007/s40820-023-01291-3.
147. Adli, N.M.; Zhang, H.; Mukherjee, S.; et al. Review—Ammonia Oxidation Electrocatalysis for Hydrogen Generation and Fuel Cells. *J. Electrochem. Soc.* **2018**, *165*, J3130. https://doi.org/10.1149/2.0191815jes.
148. Qiu, H.; Jian, J.; Huang, J.; et al. A High-Entropy Carbonate Hydroxide as a High-Efficient Tri-Functional Electrocatalyst for OER/ORR/MOR. *Mater. Today Energy* **2025**, *49*, 101847. https://doi.org/10.1016/j.mtener.2025.101847.
149. Castañeda-Morales, E.; Peralta-Cruz, J.O.; Ruiz-Zepeda, F.; et al. Electrochemical Reduction of NO_3^- to NH_3 Using Defect-Rich TiO_2 Support Loaded with CuNi Catalysts: Differential Electrochemical Mass Spectrometry Insights. *Mater. Today Energy* **2024**, *41*, 101525. https://doi.org/10.1016/j.mtener.2024.101525.
150. Gao, X.; Dai, S.; Teng, Y.; et al. Ultra-Efficient and Cost-Effective Platinum Nanomembrane Electrocatalyst for Sustainable Hydrogen Production. *Nano Micro Lett.* **2024**, *16*, 108. https://doi.org/10.1007/s40820-024-01324-5.
151. Zhang, Y.; Jiang, Y.; Abdukayum, A.; et al. Recent Advances in Selenide-Based Electrocatalysts for Hydrogen/Oxygen Evolution Reaction: From Mechanism and Synthesis to Application. *Mater. Today Energy* **2024**, *44*, 101641. https://doi.org/10.1016/j.mtener.2024.101641.
152. Zhou, P.; Li, W.; Lan, J.; et al. Electroredox Carbene Organocatalysis with Iodide as Promoter. *Nat. Commun.* **2022**, *13*, 3827. https://doi.org/10.1038/s41467-022-31453-7.
153. Zhu, C.; Ang, N.W.; Meyer, T.H.; et al. Organic Electrochemistry: Molecular Syntheses with Potential. *ACS Cent. Sci.* **2021**, *7*, 415–431. https://doi.org/10.1021/acscentsci.0c01532.
154. Yan, M.; Kawamata, Y.; Baran, P.S. Synthetic Organic Electrochemical Methods Since 2000: On the Verge of a Renaissance. *Chem. Rev.* **2017**, *117*, 13230–13319. https://doi.org/10.1021/acs.chemrev.7b00397.
155. Francke, R.; Little, R.D. Redox Catalysis in Organic Electrosynthesis: Basic Principles and Recent Developments. *Chem. Soc. Rev.* **2014**, *43*, 2492–2521. https://doi.org/10.1039/C3CS60464K.
156. Tamirat, A.G.; Guan, X.; Liu, J.; et al. Redox Mediators as Charge Agents for Changing Electrochemical Reactions. *Chem. Soc. Rev.* **2020**, *49*, 7454–7478. https://doi.org/10.1039/D0CS00489H.
157. Karim, A.V.; Nidheesh, P.V.; Oturan, M.A. Boron-Doped Diamond Electrodes for the Mineralization of Organic Pollutants in the Real Wastewater. *Curr. Opin. Electrochem.* **2021**, *30*, 100855. https://doi.org/10.1016/j.coelec.2021.100855.
158. Clematis, D.; Panizza, M. Application of Boron-Doped Diamond Electrodes for Electrochemical Oxidation of Real Wastewaters. *Curr. Opin. Electrochem.* **2021**, *30*, 100844. https://doi.org/10.1016/j.coelec.2021.100844.
159. Bejan, D.; Guinea, E.; Bunce, N.J. On the Nature of the Hydroxyl Radicals Produced at Boron-Doped Diamond and Ebonex® Anodes. *Electrochim. Acta* **2012**, *69*, 275–281. https://doi.org/10.1016/j.electacta.2012.02.097.

160. Sun, Y.; Xue, Z.; Liu, Q.; et al. Modulating Electronic Structure of Metal-Organic Frameworks by Introducing Atomically Dispersed Ru for Efficient Hydrogen Evolution. *Nat. Commun.* **2021**, *12*, 1369. https://doi.org/10.1038/s41467-021-21595-5.
161. Liao, P.-Q.; Shen, J.-Q.; Zhang, J.-P. Metal–Organic Frameworks for Electrocatalysis. *Coord. Chem. Rev.* **2018**, *373*, 22–48. https://doi.org/10.1016/j.ccr.2017.09.001.
162. Wei, Y.-S.; Zhang, M.; Zou, R.; et al. Metal–Organic Framework-Based Catalysts with Single Metal Sites. *Chem. Rev.* **2020**, *120*, 12089–12174. https://doi.org/10.1021/acs.chemrev.9b00757.
163. Wei, L.; Dai, J.; Qin, S.; et al. Two-Dimensional Materials for High-Current-Density Seawater Electrolysis. *Green Chem.* **2025**, *27*, 8755–8776. https://doi.org/10.1039/D5GC01687H.
164. Tian, H.; Zhang, H.; Zhu, Z.; et al. Near-Unity Solar Reflectance and Mid-Infrared Transparency via Microwave-Engineered 2D Y_2O_3 for Passive Radiative Cooling. *J. Mater. Chem. A* **2025**, *13*, 39330–39339. https://doi.org/10.1039/D5TA05882A.
165. Cheng, S.; Zhang, H.; Zhu, Z.; et al. Opaque, Transparent, and Colored Low-Emissivity Materials for Mid-Infrared Thermal Management. *J. Mater. Chem. A* **2025**, *13*, 38585–38608. https://doi.org/10.1039/D5TA05910K.
166. Wang, M.; Wang, Y.; Liu, J.; et al. Integration of Advanced Biotechnology for Green Carbon. *Green Carbon* **2024**, *2*, 164–175. https://doi.org/10.1016/j.greenca.2024.02.006.
167. Wang, R.; He, M.; Zhang, Z.; et al. Photodynamic Therapy Promotes Hypoxia-Activated Nitrogen Mustard Drug Release. *Smart Mol.* **2024**, *2*, e20240010. https://doi.org/10.1002/smo.20240010.